SMOS-IC data record of soil moisture and L-VOD: Historical development, applications and perspectives

Jean-Pierre Wigneron, Xiaojun Li, Frédéric Frappart, Lei Fan, Amen Al-Yaari, Gabrielle de Lannoy, Xiangzhuo Liu, Mengjia Wang, Erwan Le Masson, Christophe Moisy

Remote Sensing of Environment 254 (2021) 112238

Contents lists available at ScienceDirect

Remote Sensing of Environment

journal homepage: www.elsevier.com/locate/rse

Review

SMOS-IC data record of soil moisture and L-VOD: Historical development, applications and perspectives

Jean-Pierre Wigneron [a,*,1], Xiaojun Li [a,1,*], Frédéric Frappart [a,b], Lei Fan [c], Amen Al-Yaari [d], Gabrielle De Lannoy [e], Xiangzhuo Liu [a], Mengjia Wang [a,f], Erwan Le Masson [a], Christophe Moisy [a]

[a] INRAE, UMR1391 ISPA, F-33140, Villenave d'Ornon, France
[b] Laboratoire d'Etudes en Géophysique et Océanographie Spatiales (LEGOS), 31400 Toulouse, France
[c] School of Geographical Sciences, Nanjing University of Information Science and Technology, Nanjing, 210044, China
[d] Sorbonne Université, UMR 7619 METIS, Case 105, 4 Place Jussieu, Paris F-75005, France
[e] Department of Earth and Environmental Sciences, KU Leuven, Heverlee, B-3001, Belgium
[f] State Key Laboratory of Remote Sensing Science, Faculty of Geographical Science, Beijing Normal University, Beijing 100875, China

ARTICLE INFO

Keywords:
SMOS-IC
Vegetation optical depth
L-VOD
Soil moisture
Biomass
Vegetation phenology

ABSTRACT

Passive microwave remote sensing observations at L-band provide key and global information on surface soil moisture and vegetation water content, which are related to the Earth water and carbon cycles. Only two space-borne L-band sensors are currently operating: SMOS, launched end of 2009 and thus providing now a 10-year global data set and SMAP, launched beginning of 2015. This study provides a state-of-the-art scientific overview of the SMOS-IC retrieval data set based on the SMOS L-band observations. This SMOS product aims at improved performance and independence of auxiliary data, key features for robust applications. The SMOS-IC product includes both a soil moisture (SM) and a L-band vegetation optical depth (L-VOD) data set which are currently at the basis of several studies evaluating the impact of climate and anthropogenic activities on aboveground carbon stocks. Since the release of the first version, the algorithm has been significantly changed in support to key applications, but no document is available to report these changes. This paper fills this gap by analyzing key science questions related to the product development, reviewing application results and presenting an extensive description of the last version of the product (version 2) considering changes in comparison to the previous version (V105). For the future it is planned to merge the SMOS and SMAP L-VOD data sets to ensure L-VOD data continuity in the event of failure of one of the space-borne SMOS or SMAP sensors.

1. Introduction

Two L-band passive microwave space-borne missions are currently monitoring the Earth surface: SMOS (Soil Moisture and Ocean Salinity) developed by ESA (European Space Agency) and SMAP (Soil Moisture Active Passive) developed by NASA (National Aeronautics and Space Administration) (Kerr et al., 2016 ; Entekhabi et al., 2010). These two instruments are operating in a full-polarization mode and have demonstrated a strong capability to monitor both the soil and vegetation features over the land surfaces at global scale (Wigneron et al., 2017). The SMOS instrument, launched end of 2009, is based on a large Y-shaped interferometric antenna allowing multi-angular observations. The multi-angular capability is key for two-parameter retrievals of soil moisture (SM) and of the L-band vegetation optical depth at nadir (L-VOD) from the inversion of the L-MEB (L-band Microwave Emission of the Biosphere) model (Wigneron et al., 2000, 2007; Kerr et al., 2012). The SMAP instrument was launched more recently (January 2015) and provides mono-angular (at the incidence angle θ of 40°) observations (Entekhabi et al., 2010; O'Neill et al., 2018). The official default SMAP retrieval algorithm relies presently on the single-channel algorithm at the vertical polarization (SCA-V) (Colliander et al., 2017; O'Neill et al., 2018) which is used to retrieve SM. In SCA-V, L-VOD is computed from the vegetation water content (VWC, kg/m^2), which is estimated from climatological values of the Normalized Difference Vegetation Index (NDVI) (O'Neill et al., 2018). The link between L-VOD and VWC is given from the linear relation L-VOD = b · VWC where values of the b-

* Corresponding author at: INRAE, UMR1391 ISPA, F-33140 Villenave d'Ornon, France.
E-mail addresses: jean-pierre.wigneron@inrae.fr (J.-P. Wigneron), xiaojun.li@inrae.fr (X. Li).
[1] These authors contributed equally to this work.

https://doi.org/10.1016/j.rse.2020.112238
Received 30 June 2020; Received in revised form 28 November 2020; Accepted 30 November 2020
Available online 19 December 2020

parameter are obtained from a land cover look up table. As SMAP does not have multi-angular capabilities, other retrieval algorithms have been developed/used to achieve simultaneous retrievals of SM and L-VOD. For instance, the multi-temporal dual channel algorithm (MT-DCA, Konings et al., 2016), based on a number of consecutive observations, has been applied to the SMAP observations (Konings et al., 2017a). Recently, the enhanced SMAP SPL2SMP-E product that offers 9-km SM and L-VOD retrievals has been released (Chaubell et al., 2020). This product is based on a modified dual channel algorithm (MDCA) applied to disaggregated brightness temperatures computed from the Backus-Gilbert interpolation (Long et al., 2019a). Exploiting the SMOS capabilities for two-parameter retrievals of SM and L-VOD, the alternative SMOS INRA-CESBIO (SMOS-IC) product has been recently developed (Fernandez-Moran et al., 2017a). The main objectives of this new algorithm were: (i) to improve performance by relying on the original and simpler algorithm initially proposed for SMOS (Wigneron et al., 2000), and (ii) to achieve maximal independence of auxiliary data; contrary to the official algorithms no modelled SM data and optical vegetation indices are used in SMOS-IC. This latter feature allows avoiding possible circularity in evaluation studies comparing modelled and remotely-sensed variables.

Both the SMOS-IC SM and L-VOD products released in version 105 (V105) have been evaluated in several studies. Recent inter-comparisons have found that the SMOS-IC, SMAP and ESA CCI (Climate Change Initiative) SM products have very good performances, each product being more or less performant depending on specific soil and vegetation conditions (Al-Yaari et al., 2019a; Ma et al., 2019; Quets et al., 2019). Inter-comparisons of the SMOS L-VOD products have also showed SMOS-IC was better related to several vegetation features and vegetation optical indices (aboveground biomass (AGB), tree height, NDVI, LAI) in terms of spatial correlation than the official Level 2 and Level 3 SMOS products (Rodriguez-Fernández et al., 2018).

The satellite L-VOD vegetation index, as measured from the SMOS or SMAP instruments, has allowed the development of many applications in fields of research related to the Earth water and carbon cycles. As quickly summarized in the following, L-VOD can be used to monitor two very distinct vegetation features: vegetation water status and biomass. From *in situ* experiments, L-VOD was found to be almost linearly related to the vegetation water content (VWC) over crop fields during the vegetation growth (Jackson and Schmugge, 1991; Wigneron et al., 1995, 2007). From numerical simulations, some studies (Ferrazzoli et al., 2002; Wigneron et al., 2017) have shown that this good relationship could be extended to woody vegetation. L-VOD, through its close relationship to VWC, depends on both the quantity of vegetation (parameterized by biomass) and its moisture content (Mg, kg/kg). Disentangling the effects of both variables on L-VOD is not straightforward but several approaches based on some hypotheses can be used. From the analysis of the diurnal and daily changes in VWC, L-VOD was used to monitor the vegetation water status (Konings and Gentine, 2016). Conversely, assuming that the yearly average of the vegetation moisture content (Mg) is relatively constant from year to year, the yearly average of L-VOD can be considered as a good proxy of aboveground vegetation biomass (AGB) (Liu et al., 2015; Brandt et al., 2018a; Chaparro et al., 2019). Direct validation at the 25 × 25 km scale is difficult and the latter assumption can only be indirectly evaluated by computing the spatial correlation between L-VOD and AGB or between changes in L-VOD *vs* changes in forest fraction over different years (Qin et al., 2020). Moreover, L-VOD-related proxies of AGB have been developed considering the seasonal dynamic of the moisture content of vegetation and assuming lower changes in Mg during the wet season(s) in the tropical forests (Qin et al., 2020). However, predawn soil and plant water potentials are tightly coupled (Slatyer, 1967) and they are both related to the vegetation moisture content across many species. Interannual soil moisture differences can occur even in tropical forests (least-water limited) which would most certainly lead to less saturated plant conditions (Brando et al., 2010). Therefore, plant saturation can be expected to be different from year to year even in the tropics. So, the use of L-VOD in AGB monitoring applications reveals the strong need for better disentangling biomass and water content effects on L-VOD across all timescales as carried out in several studies (Konings et al., 2019; Momen et al., 2017; Zhang et al., 2019). VOD has generally been retrieved at relatively high frequency bands; most generally at C- and X-bands corresponding, respectively, to a frequency (f) of ~6 and 10 GHz and to a wavelength (λ) of ~3 and 6 cm (Moesinger et al., 2020). Conversely, L-VOD is retrieved at a relatively low frequency (L-band, f = 1.4 GHz, λ ~ 20 cm). VOD is depending on frequency: the lower the frequency, the better the penetration capabilities of the microwave radiations within the canopy layer. The VOD index retrieved at L-band (L-VOD) is thus better related to the vegetation features of the whole canopy layer, including the woody component, while the high-frequency VOD products (at C- and X-bands) are more related to top-of-the-canopy vegetation features (Brandt et al., 2018a; Rodriguez-Fernández et al., 2018).

In this context, the SMOS and SMAP L-VOD indices have been used in a number of application studies and only those related to the SMOS-IC product were considered here. In particular, the SMOS-IC L-VOD index whose time series exceeds 10 years now, was found to be a key index to evaluate the inter-annual variations in the aboveground biomass (AGB) stocks. Several studies have been carried out recently on that topic over sub-Saharan Africa (Brandt et al., 2018a), southern China (Tong et al., 2020), Europe (Bastos et al., 2020), and the pan-tropics (Bastos et al., 2018; Fan et al., 2019; Wigneron et al., 2020). L-VOD has also been a key vegetation index to reveal specific hydraulic features of dry tropical forests in the Miombo area (Tian et al., 2018). Following these initial and pioneer studies, the number of studies based on the SMOS-IC L-VOD index is growing quickly in several fields of applications.

The technical details of the original SMOS-IC approach have been first presented by Fernandez-Moran et al. (2017a) and the optimisation of the soil and vegetation parameters has been analyzed in Fernandez-Moran et al. (2017b). Since the first version (V105), several changes have been applied to the original SMOS-IC retrieval algorithm and several versions have been released, leading to the production of the current version (V2). However, none of these changes have been described and analyzed to date and no reference paper of the present SMOS-IC product is available. In this paper, we filled this gap by providing (i) a review of the SMOS-IC algorithm and of its main applications and (ii) a presentation and an evaluation of the most recent SMOS-IC version (V2) against reference remote sensing, modelled and *in situ* data sets. Eventually, we analyzed key points of the data set requiring improvements and presented perspectives.

2. SMOS-IC: History, rationale, objectives

2.1. Before the SMOS launch

SMOS-IC is based on the retrieval algorithm which was proposed originally by Wigneron et al. (2000) in support to the answer to the Call for Earth Explorer Opportunity Missions from ESA (European Space Agency) led by Y. Kerr in 1998. The original algorithm (referred to as L_{2P} in the following) relied on the two-parameter inversion of the L-MEB model to retrieve simultaneously SM and L-VOD from multi-angular microwave brightness temperature (T_B) measurements at L-band (Wigneron et al., 1995, 2007). As for most microwave remote sensing algorithms, L_{2P} considered homogeneous pixels.

The SM and L-VOD retrievals are based on an iterative approach minimizing a cost function (*CF*) which accounts for (i) the Root Mean Square Difference (RMSD) between measured (T_{Bmes}) and modelled (T_B*) data for all available T_B observations and (ii) *a priori* information

available on the retrieved parameters (Pulliainen et al., 1993; Wigneron et al., 2003):

$$CF = \frac{\sum (TB_{mes} - TB^*)^2}{\sigma(TB)^2} + \sum_{i=1}^{2} \frac{\left(P_i^{ini} - P_i^*\right)^2}{\sigma(P_i)^2} \quad (1)$$

where the sum of the differences between measured (T_{Bmes}) and simulated (T_B*) brightness temperatures is computed from observations over the range of available incidence angles (θ) and for both Horizontal (p = H) and Vertical (p = V) polarizations; σ(T_B) is the standard deviation associated with the brightness temperature measurements. The second term of the equation corresponds to the background information, in the form of an *a priori* estimate, which is important to make the minimization process a well-posed problem. In that term, P_i* (SM* and L-VOD*, respectively for $i = 1, 2$) is the value of retrieved SM or L-VOD; P_i^{ini} (SM^{ini} and $L\text{-}VOD^{ini}$, respectively for $i = 1, 2$) is the initial value of SM or L-VOD in the retrieval process and corresponds to an *a priori* (or "first guess") estimate; σ(P_i) is the standard deviation associated with this estimate. In SMOS-IC V2, $L\text{-}VOD^{ini}$ is computed from previous values of retrieved L-VOD (as presented later in Eq. (2)) constraining the L-VOD value to relatively low changes from overpass to overpass.

The multi-angular algorithm (L_{2P}) proposed by Wigneron et al. (1995), defined from tower-based observations with fixed ranges of incidence angles, was extended by Wigneron et al. (2000) to account for the specific multi-angular capabilities of the aperture synthesis radiometer of the SMOS mission. For this latter instrument, each pixel on the Earth can be observed for a range of incidence angles as the satellite moves along its track. This range of incidence angles is not constant as it depends on the distance between the pixel and the sub-satellite path. This range is maximal in the central part of the Field of View (FOV) and minimal at the edge of the FOV (here, by FOV we refer more precisely to the extended alias-free FOV (EAF-FOV)). The uncertainties associated with the retrievals based on observations acquired at the edge of the FOV are thus larger than those for retrievals based on observations in the central part of the FOV (where more available observations allow to constrain more efficiently the retrieval process). However, it is important to consider all observations, even those at the edge of the FOV, to improve the revisit frequency of the SMOS retrievals (Wigneron et al., 2000). Several 1-, 2- or 3-Parameter retrieval approaches were evaluated, considering retrievals of SM only (1-P retrievals) and simultaneous retrievals of SM and L-VOD (2-P retrievals) and of SM, L-VOD and surface temperature (3-P retrievals). The main idea developed in Wigneron et al. (2000) and which is now currently used in several multi-orbit retrievals (Kerr et al., 2016; Konings et al., 2017a) is that L-VOD varies relatively slowly in time and that it can be correctly estimated using a revisit time of about 5 to 10 days. So, 2-P retrievals of SM and L-VOD can be done in the central part of the FOV and in a second step, the estimate of L-VOD obtained from this 2-P retrieval can be used as a first guess (VOD^{ini} in Eq. (1)) to retrieve only SM (1-P retrieval) at the edges of the FOV. Several variations of this main idea can be developed in order to find the best compromise between the accuracy of the retrievals (using mainly 2-P retrievals from observations made in the central part of the FOV) and the revisit time of the SM and L-VOD retrievals.

Relying on these foundations and on the L-MEB inversion, the official ESA/SMOS Level 2 algorithm (referred to as L2 in the following) was developed during the 2000s (Kerr et al., 2012). In comparison to the "original" L_{2P} algorithm based on the L-MEB inversion considering homogeneous pixels, several changes have been considered in the L2 algorithm. It is not possible to list all of them, but one of the most important is that several approaches have been implemented in L2 to account for the pixel heterogeneity. To summarize the main features of L2 *vs* SMOS-IC (see detailed information in Supplementary about L2), we highlight that the L2 retrievals (i) are computed only over a fraction of the pixel (the "dominant" fraction), while the contribution of the default fraction (such as forests, forested areas, barren land (rocks), water bodies, urban areas, permanent ice, and snow) is modelled (ii) involve a complex processing including ancillary information (modelled SM, land use and Leaf Area Index (LAI) maps), a decision tree and a convolution process with the antenna pattern, to model the contribution from the "default" fraction. Most importantly, modelled SM from ECMWF (European Centre for Medium-Range Weather Forecasts) ERA-Interim and MODIS LAI (*Cf* Eq. 17 in Kerr et al., 2012) are used in some mixed pixels to compute the default T_B contribution; the use of these ancillary data is limiting potential applications of the L2 products as discussed below.

2.2. After the SMOS launch

After the SMOS launch, the official L2 SM and L-VOD products have been rapidly available for the scientific community and large inter-comparison studies of the SM products have been published (Al-Yaari et al., 2014). In parallel, studies based on the non-official L_{2P} algorithm have continued. For instance, L_{2P} was applied to Level 1-C T_B data over the VAS site (Valencia Anchor Station, Spain), one of the main SMOS calibration/validation sites in Europe (Wigneron et al., 2012). It was found the retrievals computed from L_{2P}, that did not consider the pixel heterogeneity, produced a much lower bias against *in situ* measurements (Bias ~ −0.06 m^3/m^3) than the official L2 products (Fig. S1). These results allowed to make recommendations to ESA about potential future improvements of the L2 algorithm. In particular, the high SM bias obtained in the L2 retrievals could be due to the fact the L2 retrievals tentatively accounted for pixel heterogeneity. For instance, if L2 retrievals are made over short vegetation ("dominant" fraction), a "heterogeneity" correction is applied through the use of ancillary data to estimate the "default" forest fraction. If the "heterogeneity" correction is erroneous, for instance if the modelled forest T_B contribution is underestimated, due to overestimated ECMWF ERA-Interim SM or underestimated L-VOD values over the forest fraction, it could lead to a large dry bias in the retrieved L2 SM values over the short vegetation fraction.

The results of these inter-comparisons between retrievals based on the non-official L_{2P} approach and the official L2 algorithm stimulated the interest of developing an alternative SMOS product. Eventually, the L_{2P} approach was implemented globally and led to the development of the SMOS-IC product, as presented in the next section.

3. SMOS-IC development

3.1. Materials

A presentation of the data sets used to optimize or evaluate the SMOS-IC product in their different versions is given here. We refer the readers to Li et al. (2020a), who evaluated a Two-Stream version of SMOS-IC, for more details.

3.1.1. ECMWF ERA-Interim and ERA5-Land modelled SM

To analyze the SMOS-IC SM data, we used two ECMWF reanalysis SM data sets of the top 0-7 cm soil layer: ERA-Interim (Dee et al., 2011) and ERA5-Land which is a replay of the land component of ERA5 (Hersbach et al., 2020). The ERA-Interim SM products have shown a very good accuracy, similar or higher than remote sensing products in inter-comparison studies made against *in situ* observations (Albergel et al., 2012, 2013; Peng et al., 2015; Zeng et al., 2015) and have been used in several reference inter-comparison studies (Al-Yaari et al., 2014, 2019a; Li et al., 2020a). In a recent study, Li et al. (2020b) have shown ERA5 SM presents higher skills than four other reanalysis SM products and a significant improvement over its predecessor (ERA-Interim). ERA5-Land (https://www.ecmwf.int/en/era5-land) was used here instead of ERA5 as it is independent of the assimilated SMOS observations and it has enhanced spatial resolution (9 km grid spacing *vs* 31 km for ERA5). We used hourly ERA5-Land SM products which was aggregated (using averaging) to the SMOS resolution over the 2014–2017 study period. As noted above, SMOS-IC SM is completely independent of both ERA-Interim and ERA5-Land SM. To be more independent in the

calibration and evaluation steps, ERA-Interim SM was used in the calibration step of SMOS-IC V2 (Section 3.3) while ERA5-Land SM was used in the inter-comparison step of SMOS-IC V2 and V105 (Section 4).

3.1.2. ISMN in situ SM data sets

To evaluate the SMOS-IC SM data, we used *in situ* measurements from all networks included in ISMN (International Soil Moisture Network; Dorigo et al., 2011) with sufficiently long SM time series over 2014–2017. This represents 738 sites from 20 networks over all continents (Table 1).

3.1.3. Aboveground biomass (AGB) data sets

Strong spatial correlation is expected between yearly average L-VOD and AGB (Brandt et al., 2018a; Wigneron et al., 2017), so that AGB is often used as an evaluation criteria of VOD products (Li et al., in press; Rodriguez-Fernández et al., 2018). Here, to evaluate the SMOS-IC L-VOD products in terms of spatial correlation with AGB, we used three different reference AGB maps, referred to as Saatchi (Saatchi et al., 2011), Globbiomass (Santoro et al., 2018) and ESA CCI (http://cci.esa.int/biomass). The Saatchi map used in the present study is an updated version corresponding to AGB *circa* 2015 (Carreiras et al., 2017). Saatchi AGB has already been used in several studies to calibrate the L-VOD/AGB relationship (Fan et al., 2019; Wigneron et al., 2020). Globbiomass is a recent AGB data set for the year 2010 which is obtained from multiple remote sensing and *in situ* observations at 100 m spatial resolution. Forest growing stock volume (GSV) is first estimated from the remote sensing observations and GSV is then converted to AGB with spatially explicit estimates of wood density and stem-to-total biomass expansion functions derived from forest inventory data sets (Yang et al., 2020). The ESA CCI AGB data set was developed within the ESA's Climate Change Initiative Biomass project which considers AGB, as SM, as an Essential Climate Variable (ECV). Global maps of AGB (Mg ha^{-1}) were developed at 500 m to 1 km spatial resolution with a relative error of less than 20% where AGB exceeds 50 Mg. ha^{-1} and for four epochs (mid 1990s, 2010, 2017 and 2018). We used here the CCI AGB data set for 2017 at a resolution of 100 m (CCI AGB D4.3, 2020).

All the three AGB estimates used here are based on optical, lidar and radar observations from multiple Earth observation satellites and inventory data sets. They are thus completely independent of SMOS-IC L-VOD, as SMOS-IC does not use ancillary information on vegetation as presented above.

3.1.4. IGBP land cover classes

As in Fan et al. (2019), the land cover classes were defined using MODIS 500 m land cover type data product (MCD12Q1) considering the International Geosphere–Biosphere Programme (IGBP) classes (Broxton et al., 2014) (Table 2).

3.1.5. MODIS LAI, NDVI

Spatial correlation between yearly average VOD and optical vegetation indices (LAI, NDVI) and temporal correlation between the seasonal variations in the VOD and optical indices are often used as an evaluation criteria of VOD products (Li et al., in press; Rodriguez-Fernández et al., 2018). To evaluate these spatial and temporal correlations, we used the NASA MODIS LAI (MOD15A2, resolution of 1 km) and NDVI (MOD13A2, 1 km) products (Collection 6, from 2014 to 2017, https://neo.sci.gsfc.nasa.gov). As for AGB, the MODIS products are independent of the SMOS-IC L-VOD product.

3.1.6. Precipitation

Precipitation data from 2014 to 2017 were obtained from NASA's Global Precipitation Measurement (GPM) IMERG Late Precipitation L3 1 day 0.1 × 0.1° (version 06) (Huffman et al., 2019). These data were used here to help interpreting the impact of rainfalls on the time series of the SMOS-IC SM and L-VOD data.

The different datasets (AGB, MODIS NDVI, precipitation) described

Table 1
In situ networks from ISMN used for the V105 and V2 evaluation. The type of the site vegetation cover is characterized with the IGBP land cover type. A total of 20 networks was used.

Network name	Country	Number of available sites	Land cover type (IGBP labels)	References
AMMA-CATCH	Niger	3	cropland/natural vegetation mosaics	Lebel et al. (2009)
ARM	USA	8	grasslands, croplands	https://www.arm.gov/
BIEBRZA-S-1	Poland	5	croplands	http://www.igik.edu.pl/en
DAHRA	Senegal	1	grasslands	Tagesson et al. (2015)
FMI	Finland	10	woody savannas	Rautiainen et al. (2012)
FR-Aqui	France	3	mixed forests	Al-Yarri et al. (2018)
HOBE	Denmark	27	croplands	http://www.hobe.dk/index.php/soil-moisture-network
MySMNet	Malaysia	5	evergreen broadleaf forests	https://ismn.geo.tuwien.ac.at/en/sites/networks/MySMNet/
OZNET	Australia	8	grasslands, croplands	Smith et al. (2012)
PBO-H2O	USA	54	evergreen needleleaf forests, grasslands, open shrublands, croplands, barren or sparsely vegetated	Larson et al. (2008)
REMEDHUS	Spain	20	croplands	Sanchez et al. (2012)
RISMA	Canada	20	croplands, cropland/natural vegetation mosaics	http://agriculture.canada.ca/SoilMonitoringStations
RSMN	Romania	15	croplands, cropland/natural vegetation mosaics	http://assimo.meteoromania.ro/
SCAN	USA	146	cropland/natural vegetation mosaics, barren or sparsely vegetated, croplands, deciduous broadleaf forests, evergreen needleleaf forests, grasslands, mixed forests, woody savannas, open shrublands	Schaefer et al. (2007)
SMOSMANIA	France	20	croplands, evergreen needleleaf forests, woody savannas, mixed forests, cropland/natural vegetation mosaics	Calvet et al. (2007)
SNOTEL	USA	200	croplands, evergreen needleleaf forests, mixed forests, grasslands, woody savannas, open shrublands	Serreze et al. (2001)

(*continued on next page*)

Table 1 (*continued*)

Network name	Country	Number of available sites	Land cover type (IGBP labels)	References
SOILSCAPE	USA	105	grasslands, open shrublands, savannas, woody savannas	Moghaddam et al. (2010)
TERENO	Germany	1	mixed forests	http://teodoor.icg.kfa-juelich.de/overview-de
USCRN	USA	91	cropland/natural vegetation mosaics, barren or sparsely vegetated, croplands, deciduous broadleaf forests, evergreen needleleaf forests, grasslands, mixed forests, woody savannas, open shrublands	Bell et al. (2013)
iRON	USA	4	grasslands	http://ironagci.blogspot.com/

here were rescaled to the SMOS 25 km × 25 km spatial resolution by simple averaging.

3.2. SMOS-IC V105

3.2.1. Features and parameterizations

The SMOS-IC product which was developed during 2015–2017 (Fernandez-Moran et al., 2017a), relied on the foundation of the L_{2P} approach presented above. In SMOS-IC, as for SMOS Level 2 (L2) and Level 3 (L3), L-VOD and SM are retrieved simultaneously from a two-parameter inversion of the L-MEB model from the multi-angular and dual-polarized SMOS observations. The initial released product (V105) provided global daily L-VOD and SM data from the descending and ascending orbits at a spatial resolution of 25 km over the period from 12 January 2010 to 31 December 2017.

SMOS-IC differs from L2 and L3 in several respects (we refer the reader to Fernandez-Moran et al. (2017a) for more details), but the main one is that SMOS-IC assumes the pixel to be homogeneous: L-VOD and SM are retrieved over the whole pixel rather than over a fraction of it. We anticipated that the L2 complexities may result in more uncertainty in the retrieval process, so that they should be carefully evaluated. SMOS-IC contributed to this evaluation by:

(1) deleting complex corrections, whose full evaluation is very difficult and which may lead to add more noise than improvement. In particular, accounting for the pixel heterogeneity can be very tricky in the specific case of SMOS: the daily SMOS observations have different angular configurations in terms of incidence angle and azimuth, so that the SMOS footprint changes from one day to the other and for each multi-angular observation.
(2) avoiding the use of a decision tree which may lead in discontinuities linked to the definition of pixel cells considered as "default" or "dominant" contributions.
(3) most importantly, developing a product as independent as possible from auxiliary data: in SMOS-IC, L-VOD and SM are retrieved without external vegetation or hydrologic products as inputs in the L-MEB inversion model. L-VOD and SM retrievals thus depend only on temperature fields from ECMWF ERA-Interim (0-7 cm soil temperature and skin temperature) for calculating the effective surface temperature (Wigneron et al., 2007) and are independent of any vegetation index and modelled SM data. This later step is very important for robust applications (especially when the objective is to improve models) and avoids circularity when evaluating remotely-sensed products against modelled ones. Advancing science and improving global models, both in terms of carbon and hydrological cycles is an objective which is often put forward to justify the remote sensing missions. However, can this objective be easily reached if modelled and remotely-sensed products are not developed independently, preventing independent inter-comparisons, evaluations and assimilation approaches?

Table 2
Eleven main IGBP classes considered in the study.

Main type		Land Cover
Woody vegetation Cover	EBF	Evergreen broadleaf forests
	DNF	Deciduous needleleaf forests
	DBF	Deciduous broadleaf forests
	MF	Mixed forests
	WS	Woody savannas
Herbaceous or sparse vegetation types	SH	Shrublands
	S	Savannas
	G	Grasslands
	C	Croplands
	CNVM	Cropland/natural vegetation mosaics
	BSV	Barren or sparsely vegetated

As SMOS-IC does not account for pixel heterogeneity, a new calibration of the soil and vegetation parameters was carried out. SMOS-IC distinguishes values of the effective scattering albedo (ω) for forest (ω = 0.06, as estimated in Parrens et al., 2017) and non-forest vegetation canopies (ω ∼ 0.1, Fernandez-Moran et al., 2017b). The effective roughness parameter H_R was estimated from the global roughness map of Parrens et al. (2016) while the roughness parameters N_{RP} (P = V, or P = H for the vertical and horizontal polarizations) were distinguished for forest ($N_{RV} = -1$; $N_{RH} = 1$) and non-forest ($N_{RV} = -1$; $N_{RH} = -1$) soils.

The input T_B data of SMOS-IC are a specific non-filtered (and non-public) version of the Level 3 T_B data provided by CATDS (Centre Aval de Traitement des Données SMOS) the French ground segment for the SMOS Level 3 and 4 data. This non-filtered option was obtained from CATDS as the official and public CATDS L3 T_B products (Al Bitar et al., 2017) used a strong filtering procedure on sun-glint effects, which led to delete T_B observations in the central part of the SMOS FOV, exhibiting characteristic central stripes in the orbital L3 T_B maps. This filtering was estimated to be too strict for SMOS-IC as it deleted many data in the central region of the FOV, a region which is the richest in terms of ranges of multi-angular T_B data. SMOS-IC used its own filtering procedure to filter out the non-filtered L3 T_B data as described in the following sections. Note that the official ESA/SMOS L2 algorithm has not been affected by this issue as it is directly based on Level 1 T_B products. In the near future, this issue should no longer affects the official L3 T_B products since as a new L3 T_B product is being released.

3.2.2. Data filtering

Data filtering is a key component associated with the SMOS-IC algorithm. This filtering has been progressively improved since the initial paper by Fernandez-Moran et al. (2017a) to support the development of applications. Data filtering is essential because data errors would affect the SMOS SM and L-VOD retrievals:

(i). errors associated with the viewing angle geometry of the interferometric antenna of SMOS; in SMOS-IC, only observations for incidence angles $>20^\circ$ and $< 55^\circ$ are kept in the retrievals, to avoid observations which are relatively noisy and inaccuracies in L-MEB for large angles. Note that this chosen range of angles corresponds relatively well to the alias free field of view (AFFOV): most of the observations for incidence lower than 20° and

higher than ~60° are out of the AF-FOV. Retrievals are implemented only when the range of angular values exceeds 10°, as a small range of angular variations correspond with observations made at the edge of the SMOS FOV which are associated with a higher uncertainty (Wigneron et al., 2000).

(ii). errors associated with the radio frequency interferences (RFI).

RFI are very present at L-band and strongly affect the SMOS T_B observations and, consequently, the SM and L-VOD retrievals. RFI may strongly vary both in space and time so that detecting and filtering them out is very difficult. Several RFI filtering procedures have been developed and combined in an effort to limit their impact on the SMOS-IC retrievals (all observations are affected, albeit to varying degrees). These corrections are detailed more specifically here, as they are key for applications and they have not been yet analyzed in detail in the literature. Contrary to L2 and L3, SMOS-IC does not use probability maps of RFI occurrence, but it provides an estimate of the actual RFI impacts.

Following Wigneron et al. (2012), the Root Mean Square Error (RMSE) value between the measured and the L-MEB modelled T_B data (referred to as TB-RMSE) is used as an index to estimate the impact of RFI on the SMOS T_B data. The rationale behind the choice of this index is that L-MEB is able to fit very well the multi-angular and dual-polarization signatures of the SMOS observations over a large variety of land surface scenes (covered by soil, vegetation, water, ice, snow, rocks *etc.* for low, medium or high topography).

So, in the absence of RFI, L-MEB will be able to fit very well the SMOS TB observations and the TB-RMSE index will be low, as it will determined primarily by the standard deviation associated with the SMOS T_B data (typically close to 3 to 4 K). Most of the differences between this lower limit value (TB-RMSE ~3–4 K) and the actual value of TB-RMSE are due to RFI effects. If there is RFI, the SMOS TB observations will be noisy (*Cf* Fig. S2) and L-MEB will be unable to provide a good fit to the SMOS multi-angular observations, leading to high TB-RMSE values. In other words, high TB-RMSE values are indicative of noisy multi-angular observations, which are, to our knowledge, mostly due to RFI effects. Based on this principle, several post-processing filtering procedures are used in SMOS-IC and they are presented below:

3.2.3. TB-RMSE daily filtering

The TB-RMSE index is used to filter out daily SMOS T_B observations strongly affected by the RFI effects: all retrievals associated with a TB-RMSE index higher than a threshold are deleted. Wigneron et al. (2012) suggested initially a threshold value of 12 K, but a stricter threshold value of 8 K is recommended now. The selection of this threshold is a compromise: decreasing the value will lead to more accurate retrievals but to less data. Following several evaluation studies, an even stricter filtering (threshold value of 6 K) has been recommended for L-VOD, as the retrieved L-VOD values were found to be more sensitive to RFI effects than the SM ones.

3.2.4. TB-RMSE spatial filtering

Daily filtering based on TB-RMSE can filter out most of obvious and strong RFI effects, but it is not 100% safe and RFI-contaminated observations may pass through it. This daily filtering can be supplemented by a spatial filtering based on annual maps of the average TB-RMSE index which are good proxies of the average RFI annual intensity. These annual maps can provide an interesting overview of the temporal dynamics of the RFI effects at global scale as shown in Fig. 1 and they can be applied to carry out a spatial filtering of pixels strongly affected by RFI effects. This spatial filtering can be applied each year (or each 6 months or even monthly) to account for temporal changes in the spatial RFI patterns. For instance, it can be noted that RFI effects strongly decreased over China in the recent years.

3.2.5. ΔL-VOD filtering

As the boresight of the SMOS antenna is forward tilted by 32.5° with respect to nadir, the observations made for the ascending (Asc) and descending (Desc) orbits do not have the same sensitivity to the RFI effects; the latter being directional. This feature is interesting to detect RFI. The rationale is that, for low RFI effects, low differences (referred to

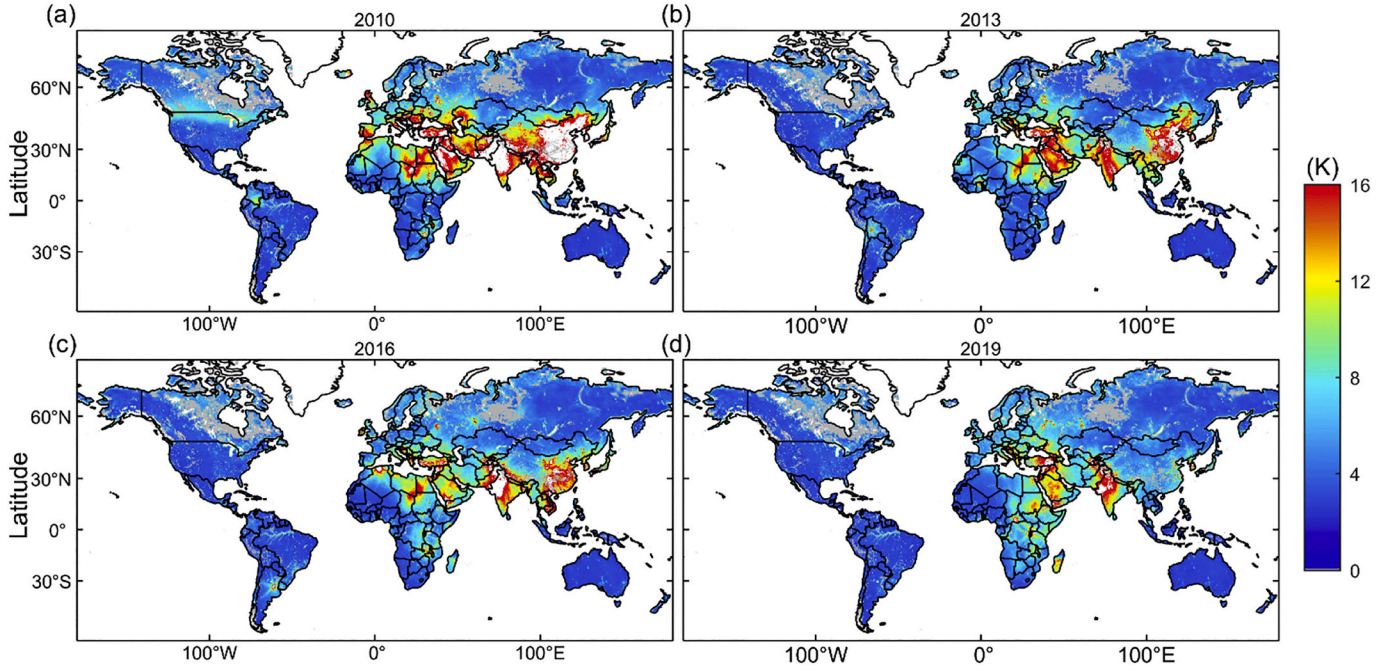

Fig. 1. Temporal dynamics of the RFI effects at global scale: annual maps of the average TB-RMSE index for (a) 2010 (b) 2013 (c) 2016 and (d) 2019. Blank areas correspond to areas where no data is available (defined here by TB-RMSE larger than 20 K); grey areas correspond to areas filtered out considering the scene flag (fraction of water bodies or urban areas or strong topography >10%, *Cf* Table 3). Very high level of RFI contamination found in China and the Arabian Peninsula in 2010 and 2013 agree well with maps based on other RFI indices (*e.g.* Soldo et al., 2016). We can note generally a decrease in the RFI effects, especially in Europe and China, but a slight increase in some regions of Africa. A large RFI pattern at the USA/Canada border in 2010–2011 disappeared.

as ΔL-VOD) between the retrieved values of L-VOD can be expected from observations made from the Asc and Des orbits at, respectively, 6 am and 6 pm local time. Non-zero values of ΔL-VOD can be expected due to (i) the change in the water content of vegetation between morning and afternoon (Konings and Gentine, 2016) and (ii) possible effects of dew and water interception by the canopy (Saleh et al., 2006). However, these differences should not be large. A very detailed analysis of the RFI event that occurred at the Canada-USA border during the 2010–2011 period (Al-Yaari et al., 2020) showed that ΔL-VOD values larger than ~0.05 are generally indicative of RFI effects affecting Asc or Desc or both Asc/Desc orbits. A threshold value of 0.05 was thus used in this study for the ΔL-VOD filtering index. Note that we focused here on L-VOD as it is, as noted above, more sensitive than SM to RFI.

3.2.6. Combined (Asc and Desc) yearly median L-VOD

From the three post-processing filtering procedures described above, it is possible to compute yearly median or average L-VOD values which are used in science applications. An additional post-processing filtering can be used to compute these median or average L-VOD values. It consists in computing them by combining the Asc and Desc L-VOD products and by selecting the least RFI-contaminated Asc and/or Desc observations. The rationale is that, as noted above, observations made for Asc and Desc orbits do not have the same sensitivity to the RFI effects. So, for a given pixel and date, the use of data for Asc or Desc orbits can be preferable. Based on this principle, the combined yearly average L-VOD product can be built as follows:

- each year, a combined L-VOD data set is built by selecting the "best" N observations estimated from either Asc or Desc orbits; "best" being defined here in terms of lower TB-RMSE values; typical values of N are N=30 and N=50,
- over each year, the median of the L-VOD values retrieved from the N "best" observations are computed.

For instance, over China, as the Asc observations are generally more contaminated by RFI than the Desc ones, the combined products over China will mainly include Desc observations. Similarly, a strong RFI event affecting mostly the Asc observations was noted at the USA/Canada border in 2010 and 2011. In that case, over that region in 2010–2011, the combined product will mainly select Desc L-VOD data, corresponding generally to lower TB-RMSE values. Note that, when applying the "combined asc/desc" method, important caution should be taken to ensure that the asc *vs* desc L-VOD data are selected similarly year to year; otherwise computation of interannual L-VOD trends could be biased.

In addition to these RFI filtering procedures, several effects associated with specific climate or topographic conditions can be filtered out using flags indicative of specific conditions. These flags, referred to as "scene" flags, are listed in Table 3.

3.3. SMOS-IC V2

Since V105, several changes have been made to develop the SMOS-IC V2 product: (i) continuous improvements in the initialization maps of L-VOD^{ini} (ii) continuous improvements in data filtering (*Cf* above section), which impacted too the computation of the L-VOD^{ini} maps (iii) evaluating the use in SMOS-IC of a first order modelling approach (2-Stream) instead of the zero-order Tau-Omega model (Li et al., 2020a). The enhanced physical background of 2-Stream allows its implementation as a unified emission model to estimate SM and VOD, snow properties and ground freeze or thaw conditions. The 2-Stream model can be easily substituted to the Tau-Omega model in Version 2 (option not evaluated here for the sake of conciseness) (iv) development of a multi-temporal (MT) approach. The development of a MT approach relies on the assumption that L-VOD varies relatively slowly in time (Wigneron et al., 2000). This assumption has been used in the SMOS L3 (Kerr et al., 2016) and in the MT-DCA SMAP retrieval algorithm (Konings et al., 2017a) where observations acquired for several dates during a moving time window are used to constrain the simultaneous retrievals of SM and VOD. We used a multi-temporal (MT) approach in V2, as it allowed adding more constraints in the retrievals by using observations for several dates, instead of only one in version V105. The MT approach could be particularly interesting in the case of SMOS as the range of the available observation angles vary from day to day. For instance, the MT approach allows to use "best" estimates of VOD, retrieved at a date when the range of multi-angular observations is optimal, to estimate a first guess value of VOD for subsequent SM & VOD retrievals (Wigneron et al., 2000).

This concept translates more concretely into the following approach which was implemented in SMOS-IC V2. In the cost function (Eq. (1)), to retrieve SM & VOD at a date t, we used an *a priori* estimate of L-VOD (referred to as L-VOD^{ini}(t)) which is computed as the average L-VOD* values retrieved from the previous N days (these previous dates are denoted here by t_{-1}, t_{-2}, … t_{-N}):

$$L\_VOD^{ini}(t) = \begin{cases} average\left(L\_VOD^{*}_{t-1}, L\_VOD^{*}_{t-2}, \cdots, L\_VOD^{*}_{t-N}\right) \text{ if available} \\ L\_VOD_{m}(t) \text{ if mean value of previous N days not available} \end{cases} \quad (2)$$

Eq. (2) means that to compute L-VOD^{ini}(t):

(i). L-VOD^{ini}(t) was set equal to the average L-VOD value computed over the time interval [t_{-1}, t_{-2}, … t_{-N}], if this average value is available. This average value may not be available for several reasons: if no retrieval is available during the N previous days (because of soil freezing in winter for instance, if all previous retrievals made during the previous N days are filtered out after quality control, *etc.*)

Table 3
Summary of the SMOS-IC filtering procedures.

Filtering type	Threshold value (indicative value that depends on applications)	Conditions of applications
RFI filtering		
TB-RMSE daily filtering	TB-RMSE <6 K or 8 K (depending on applications)	for each pixel and each date
TB-RMSE annual filtering	annual average TB-RMSE <6 K or 8 K	for each pixel and each year
ΔL-VOD daily filtering	ΔVOD <0.1	for each pixel and each date
ΔL-VOD annual filtering	annual average ΔVOD <0.1	for each pixel and each year
Combined yearly L-VOD data set (Asc & Desc)	-select N = 30 or N = 50 "best"* yearly observations	for each pixel and each year
Combined yearly median L-VOD (Asc & Desc)	-compute median of the N "best" L-VOD values	
Scene flags	(*Cf* Supplementary data format)	
Topography flag	low-, medium- or high-topography	for each pixel (Mialon et al., 2008)
Contaminated scene (water bodies, urban area, ice)	summed fraction <10%	for each pixel and each date
Frozen conditions	ERA-Interim top soil layer temperature > 273 K	for each pixel and each date
Data filtering**		
SM range	0 ≤ SM ≤ 1; SM (m^3/m^3)	
L-VOD range	0 ≤ L-VOD ≤ 2	

* "best" being defined here in terms of lower TB-RMSE values;
** Filtering is done after computing yearly average, as negative daily SM or L-VOD values are not physical but are numerically possible in arid areas and should not be deleted before computing yearly averages.

(ii). otherwise, L-VOD^{ini}(t) was set equal to L-VOD$_m$(t), where L-VOD$_m$(t) is the average monthly L-VOD value of the month corresponding to date t. L-VOD$_m$ is a 12-element vector including average monthly L-VOD values computed for each pixel over 2012–2019. The latter period was used as, starting from 2012, the retrieved VOD data was found to be no more sensitive to the initial first guess VOD value used at the very beginning of the retrieval process, *e.g.* beginning of 2010.

In version 2, all the other model parameters and inputs to the cost function in Eq. (1) are consistent with the first version (V105) of SMOS-IC and are defined in Fernandez-Moran et al. (2017a).

In Eq. (2), the value of N (N = 5, 10, 15… 30 days for instance) cannot be too small to ensure a good quality of the mean value of the retrieved L-VOD values before date t; it cannot be too large too to ensure that L-VOD did not change much over the period of N days. In reality, following the time variations in VWC, L-VOD may change quickly from one day to the other. For instance, VWC may present quick temporal changes at the scale of a few hours, in relation with changes in the vegetation water status (for instance during a rainfall event following a drought period) or in the intercepted water storage (Saleh et al., 2006). However, these temporal changes can be considered as relatively small at large scale as the SMOS footprint includes a variety of vegetation types and conditions. This hypothesis was further supported by the results of Tian et al. (2018) who found a small amplitude in the L-VOD annual changes (less than 0.1 in general at global scale). Note that this assumption contrasts with recent studies that directly investigated non-negligible AMSR2 (Advanced Microwave Scanning Radiometer 2) and SMAP VOD changes over the day and after rain events. Such changes over the day and post rainfall are attributed to rehydration and water loss patterns (Feldman et al., 2018; Konings et al., 2016, 2017b). The differences found between SMOS and the other SMAP and AMSR sensors could be related to the specific SMOS antenna viewing system that limit its capability to monitor accurately the changes between the ascending and descending observations (Wigneron et al., 2018). Note that here, contrary to some other MT retrieval approaches, the assumptions made in V2 are not so strict: we only assume slow time changes in L-VOD and we do not need to make the hypothesis that L-VOD is constant over a moving time window (typically one week).

To develop IC V2, several parameters constraining the retrievals were optimized. The main key parameters to consider were:

(1) N (days), which corresponds to the length of the time interval [t_{-1}, t_{-2}, … t_{-N}] used to compute L-VOD^{ini}.
(2) the TB-RMSE (K) value (referred to as TB_R) used to filter the retrieved L-VOD values within the [t_{-1}, t_{-2}, … t_{-N}] interval.
(3) σ_{VOD}, the standard deviation value used in the last term of Eq. (1) that constrains the L-VOD retrievals; this value parameterizes the confidence we have in the estimated first guess L-VOD^{ini} value.

As discussed above, at large spatial scale, the "true" value of the SM and L-VOD data that drives the microwave measurements cannot be estimated (Gruber et al., 2020): only proxies which are more or less pertinent for specific soil and vegetation conditions can be found. The parameter optimization was carried out in this study considering only one criterion for the retrieved SM and L-VOD parameters (*Cf* section 3.1):

- for SM, as a criterion, we used the global ERA-Interim SM simulations.
- for L-VOD, as a criterion, we used the spatial correlation between yearly averages of L-VOD and Saatchi AGB.

The evaluation was made here using classical statistical metrics as in Li et al. (2020a): correlation in terms of coefficient of correlation (R), Root Mean Square Error (RMSE, m^3/m^3), unbiased Root Mean Square Error (ubRMSE, m^3/m^3) and bias (m^3/m^3). To obtain best scores in the SM and L-VOD retrievals considering the above criteria, we evaluated possible values of N, σ_{VOD} and TB_R. Based on previous studies (Wigneron et al., 2007, 2012), we evaluated only a limited number of cases corresponding to N = 10 or 20 days, σ_{VOD} = 0.05 or 0.1 and TB_R = 6 or 8 K. So, 8 "retrieval algorithms" corresponding to 8 cases corresponding to different values of N, σ_{VOD} and TB_R were evaluated here by comparison to the ancillary data sets (ERA5-Land SM for SM and Saatchi AGB for L-VOD). Based on this analysis, the differences in the performances of IC for these 8 different algorithms were generally small (Table S1–5). We selected for V2 the algorithm providing best results (*i.e.* N = 10 days, σ_{VOD} = 0.05 and TB_R = 6 K; very similar results obtained for N = 20 days and σ_{VOD} = 0.1). Based on this approach, circularity that may happen when considering the same ancillary data for the "calibration" and "evaluation" steps is very limited in this study. Moreover, ECMWF ERA-Interim SM was used for calibration and ECMWF ERA5-Land SM was used for validation and even though these two SM datasets are very similar, they are not the same.

4. SMOS-IC evaluation

SMOS-IC is a SM and L-VOD product and so the product evaluation generally benefits from a simultaneous evaluation of both the SM and L-VOD products, contrarily to other RS microwave products where evaluation is generally focused separately on either the SM or the VOD product. Our philosophy here is that improved L-VOD products are beneficial to SM retrievals and *vice versa*. Since the original studies presenting the retrieval method (Wigneron et al., 2000, 2012), several papers have evaluated the first version (V105) of SMOS-IC in terms of SM and L-VOD products. A summary of these evaluations is given here and, in a second step, we evaluated the "improvements" obtained with the new version (V2).

The criteria used in the SMOS-IC evaluation have limitations and missed a one to one representation of SM or L-VOD at a resolution of ~25 km. For instance, (i) *in situ* data are very interesting (Dong et al., 2020), but are at point scales and not representative of microwave satellite scales (Crow and Wood, 2002) (ii) AGB and NDVI are limited because they only provide biomass proxies and water content changes that can be out of phase with the LAI and NDVI metrics (Tian et al., 2018). So, the evaluation made in this work used several criteria for both the SM and VOD retrievals; a multi-criteria evaluation being more able to reveal strengths and weaknesses of the updated SMOS-IC version. Moreover, in the following, the term "improvement" will not be used. We will use instead terms as "closer to benchmarks/proxies" or "better scores" as the evaluation data sets used in this study have errors and do not represent integrated satellite data at a resolution of 25 km × 25 km.

4.1. SMOS-IC V105 evaluation

4.1.1. Soil moisture

Fernandez-Moran et al. (2017a) have evaluated the IC V105 and L3 SM products against ERA-Interim SM, a reference SM product at global scale (Albergel et al., 2012). They found IC V105 presented better scores, in terms of both correlation (R), over almost 90% of the studied pixels, and unbiased Root Mean Square Error (ubRMSE); similar dry bias patterns being noted for both products. This good performance was all the more surprising and satisfying as IC V105 SM is, contrary to L3 SM, completely independent of ERA-Interim SM. This initial study was limited to a comparison with modelled data, but since then, more detailed studies have been published. For instance, Al-Yaari et al. (2019a) have evaluated five recently developed/reprocessed microwave satellite soil moisture products against *in situ* measurements from ISMN. The study carried out over 2015–2017 included five SM products: SMOS-IC (V105), SMOS L2 (V650), SMOS L3 (V300), SMAP (Level3, V4) and CCI (V04.2). IC V105 and SMAP presented very good and relatively similar global performances and, in particular, IC V105 presented high

performances in terms of correlation computed from SM anomalies, which are related to the day to day variability of *in situ* SM. Ma et al. (2019) extended the inter-comparison and found globally best correlation results for SMAP and CCI (European Space Agency (ESA) Climate Change Initiative) products, followed by IC V105; with IC V105 achieving the highest R value for dense vegetation conditions. IC V105, as the other SMOS official products, presented generally a dry bias. Even if bias is an interesting criterion, it was considered as the least important performance metric in the SMOS-IC SM algorithm calibration processes (Fernandez-Moran et al., 2017a). Several reasons led to this choice: (i) it is very difficult to define an absolute SM value over mixed pixels at 25 km × 25 km. At such a coarse resolution, SM represents an effective value whose absolute level can be different depending on the application (Gruber et al., 2020). (ii) As noted by Al-Yaari et al. (2019a), bias strongly depends on the auxiliary data sets and parameters used to compute absolute SM values (*e.g.* porosity data for ASCAT, modelled data sets for CCI). (iii) Remotely-sensed at different frequencies, modelled and *in situ* SM data sets are estimated or simulated for different sampling depths (which may vary with the moisture conditions), making inter-comparisons of absolute SM values difficult. (iv) Many applications use relative SM indices rather than SM absolute values; for instance, bias is generally removed prior to assimilation, or else estimated as part of the assimilation system (De Lannoy and Reichle, 2016). To complete this section, we list in a non-exhaustive fashion some other studies including evaluations or inter-comparisons related to the SMOS IC SM data: Fan et al. (2020), Kim et al. (2020) and Zhang et al. (2020) at the global scale; Li et al. (2020a) for the 2-Stream version; Liu et al., in press, in Tibet; Sadeghi et al. (2020) in relation with SM data sets computed from GRACE observations; Quets et al. (2019) based on the SMAP cal/val sites, *etc.*

4.1.2. L-VOD

Contrarily to SM, few studies have inter-compared the VOD products retrieved from different microwave space-borne sensors. The evaluation is more difficult than for SM, as no data can be considered as a reference for L-VOD. As noted in introduction, VOD and more particularly L-VOD can be linearly related to vegetation water content (VWC, kg/m^2). A strong linear relationship: L-VOD = b · VWC, with b ~ 0.12 (±0.03) was computed by Jackson and Schmugge (1991). A relatively good relationship was obtained too between retrieved L-VOD values and LAI: L-VOD = b' LAI + b", with b' ~ 0.06 (Wigneron et al., 2017). However, these relationships have been mainly investigated for crops and they are relatively linear only during the vegetation growth and not during crop senescence (Wigneron et al., 2004). From space-borne observations, several studies have also found good relationships between VOD and vegetation indices, as NDVI (normalized difference vegetation index), EVI (enhanced vegetation index), LAI (Leaf Area Index), computed from optical remote sensing observations (Grant et al., 2016; Lawrence et al., 2014). However, temporal correlation between VOD and vegetation indices should also be evaluated carefully considering time lags of several weeks or months that occur between different climate and vegetation variables (SM, VOD, LAI, EVI) in some ecosystems as was found over dry and wet tropical forests (Jones et al., 2014; Tian et al., 2018). A lower time lag of ~19 days was found for crops in the USA (Lawrence et al., 2014). VOD can also be evaluated by comparing its spatial variations against AGB maps (Liu et al., 2015; Brandt et al., 2018a). Moreover, as plant saturation may change from year to year confounding effects of biomass, one can attempt to control for saturation by using wet season 90th or 95th percentile of L-VOD (Qin et al., 2020).

In summary, evaluating the quality & accuracy of the retrieved VOD products is not straightforward and only indirect and approximate assessments can be done. We tentatively list the main ones here: (i) spatial correlation between yearly average of VOD and AGB at continental scales; this criterion being more appropriate for woody vegetation (ii) temporal correlation between VOD and vegetation optical indices (as NDVI, EVI, LAI, *etc.*); considering the saturation of the optical indices in densely vegetated area, this criterion is more appropriate for herbaceous vegetation. Temporal correlations can be computed on raw data, climatology data using moving average or anomalies (Al-Yaari et al., 2019a; Dong et al., 2020). Here, to limit the impact of noise of the daily raw L-VOD data, correlations were computed on a bi-monthly basis which corresponds to the format of the used MODIS NDVI data sets; (iii) spatial correlation between VOD and vegetation optical indices (as NDVI, EVI, LAI, *etc.*), considering yearly average or daily values at continental scales; this criterion being also more appropriate for herbaceous vegetation.

In an initial study at global scale, Fernandez-Moran et al. (2017a) found higher temporal and spatial correlation between L-VOD and MODIS NDVI for SMOS-IC *vs* SMOS-L3. In a larger inter-comparison study considering the criteria listed above with the SMOS-L2 and -L3 products, Rodriguez-Fernández et al. (2018) have confirmed the good performances of the SMOS-IC data set for vegetation studies. Rodriguez-Fernández et al. (2018) and Brandt et al. (2018a) were the first to analyze the relationship between SMOS-IC L-VOD and biomass. This relationship was found to be almost linear and to present low signs of saturation at high levels of biomass, contrarily to results obtained from higher frequency products as C- and X-VOD (C- and X-VOD refer here to VOD products estimated from observations at C- and X-bands). This result was expected as microwave radiations are impacted by extinction effects (through attenuation and scattering effects) as they propagate through the vegetation canopy. These extinction effects increase with frequency, making low frequency observations at L-band more suitable for monitoring SM over dense vegetation canopies than observations at higher frequencies such as C- and X-bands (Al-Yaari et al., 2014). These effects explain the lower saturation effects obtained at L-band *vs* X-band when comparing L-VOD with AGB or aboveground carbon (AGC) stocks (Fig. S3).

4.2. SMOS-IC V2 evaluation

No evaluation study has yet been published for SMOS-IC V2 and we focused here on the changes of the new (V2) version *vs* the previous (V105) one. To that aim, we inter-compared the SMOS-IC SM and L-VOD products of V105 and V2 using all the five criteria presented in Section 3.3. The present analysis is carried out over a 4-year period (2014–2017) which is large enough to analyze the seasonal variations in both SM and L-VOD, and short enough to correspond to relatively homogeneous RFI conditions; considering the changes in the spatio-temporal patterns in RFI (Fig. 1), a longer evaluation time period would make the interpretation of performance results more complex. Note that, in this section, we did not expect a large improvement (associated with a large change in the values of the correlation and ubRMSE metrics) in the performance of V2 *vs* V105. There are two main reasons: (i) V105 has already been found to be a performant product and it is likely the performance metrics of SMOS-IC, SMAP and ASCAT in evaluation studies are close to maximum now; (ii) there is no accurate and large scale reference SM data set at the spatial resolution of 25 km × 25 km. So, the true performance of the different SM products cannot be evaluated in a very accurate and definitive way (Gruber et al., 2020).

4.2.1. Soil moisture

V2 was closer to the reference SM values (modelled ERA5 Land and *in situ* ISMN SM data) than V105, considering both correlation (R) and ubRMSE criteria for all IGBP vegetation types (Fig. S4, Tables 4 & 5). Comparing globally with the ERA5-Land SM data, when upgrading from V105 to V2 the average ubRMSE decreased from 0.058 m^3/m^3 to 0.055 m^3/m^3 and the median correlation (R) increased from 0.65 to 0.66 (Table 4). Interestingly, when using *in situ* ISMN SM data instead of ERA5-Land SM data as a reference, better scores were obtained for both V105 and V2 and the differences between V105 and V2 were slightly larger: globally, the average ubRMSE decreased from 0.062 m^3/m^3 to 0.059 m^3/m^3 and the median correlation coefficient (R) increased from

Table 4
Performance metrics in the soil moisture inter-comparison of SMOS-IC V105 and SMOS-IC V2 against ERA5-Land SM (2014–2017) in terms of temporal correlation coefficient (R), unbiased RMSE (ubRMSE, m^3/m^3), Bias (m^3/m^3) and RMSE (m^3/m^3), for different vegetation types, as defined by the IGBP land cover classification; overall (last column) corresponds to all pixels at global scale after filtering with the scene flag.

	Version	ENF	EBF	DNF	DBF	MF	SH	WS	S	G	C	CNVM	BSV	Overall
R	V2	0.37	0.34	0.29	0.59	0.40	0.69	0.74	0.81	0.73	0.73	0.68	0.57	0.66
	V105	0.29	0.29	0.22	0.57	0.35	0.69	0.70	0.79	0.72	0.72	0.67	0.56	0.65
ubRMSE	V2	0.064	0.069	0.061	0.064	0.064	0.049	0.065	0.059	0.052	0.057	0.057	0.026	0.055
	V105	0.079	0.077	0.079	0.073	0.076	0.051	0.073	0.060	0.053	0.058	0.060	0.027	0.058
Bias	V2	−0.128	−0.184	−0.221	−0.148	−0.181	−0.058	−0.097	−0.120	−0.130	−0.145	−0.163	0.016	−0.110
	V105	−0.117	−0.184	−0.199	−0.142	−0.173	−0.054	−0.092	−0.118	−0.129	−0.145	−0.160	0.016	−0.106
RMSE	V2	0.148	0.198	0.228	0.164	0.194	0.086	0.122	0.136	0.142	0.157	0.175	0.036	0.130
	V105	0.146	0.201	0.214	0.161	0.192	0.083	0.122	0.135	0.142	0.158	0.173	0.037	0.129

Table 5
Same as Table 4, except that the soil moisture inter-comparison is made between SMOS-IC V105 and SMOS-IC V2 against the ISMN *in situ* SM (738 sites from 20 networks, 2014–2017).

	Version	ENF	EBF	DBF	MF	SH	WS	S	G	C	CNVM	BSV	Overall
R	V2	0.63*	0.54*	0.65*	0.70*	0.62*	0.63^{NS}	0.86*	0.66*	0.68*	0.72*	0.59*	0.68*
	V105	0.58	0.48	0.65	0.62	0.61	0.62	0.85	0.64	0.67	0.72	0.58	0.66
ubRMSE	V2	0.069*	0.070*	0.064*	0.055*	0.046*	0.058*	0.060*	0.061*	0.057*	0.054*	0.041^{NS}	0.059*
	V105	0.076	0.080	0.070	0.066	0.047	0.069	0.063	0.063	0.059	0.056	0.042	0.062
Bias	V2	0.010	0.024	−0.082	−0.041	−0.021	0.036	−0.002	−0.073	−0.053	−0.095	−0.034	−0.048
	V105	0.013	0.021	−0.074	−0.038	−0.020	0.042	0.000	−0.071	−0.051	−0.091	−0.033	−0.045
RMSE	V2	0.095	0.072	0.101	0.106	0.059	0.109	0.072	0.101	0.095	0.114	0.056	0.093
	V105	0.101	0.083	0.108	0.104	0.060	0.109	0.075	0.101	0.095	0.113	0.056	0.094

* indicates that the difference between the two versions of SMOS-IC is significant at least at the 0.05 probability level using one-way ANOVA test. 'NS' indicates non-significant difference at the 0.05 probability level.

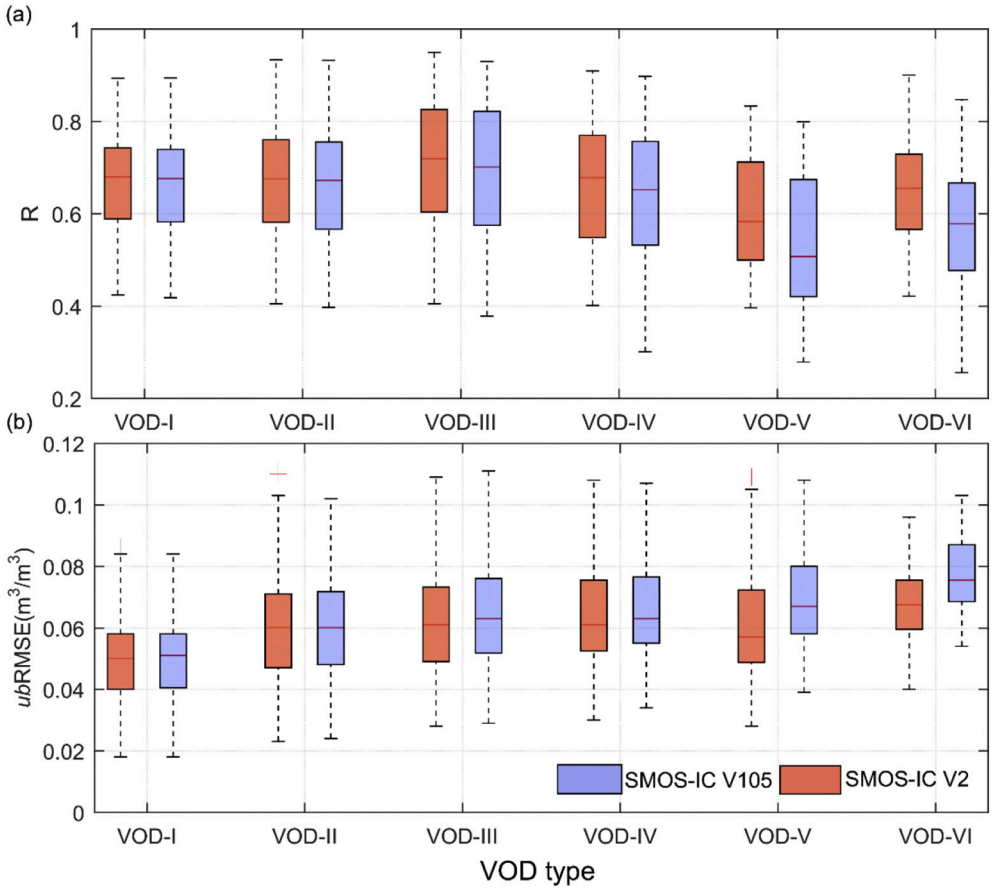

Fig. 2. Box plots of (a) correlation (R) and (b) ubRMSE for the relationship between SMOS-IC V105 (blue) or V2 (red) SM and *in situ* SM (2014–2017) for different L-VOD intervals corresponding to different "biomass" intervals: VOD-I: 0– 0.1 (n = 88 stations); VOD-II: 0.1– 0.2 (n = 199 stations); VOD-III: 0.2– 0.3 (n = 245 stations); VOD-IV: 0.3– 0.4 (n = 93 stations); VOD-V: 0.4– 0.5 (n = 73 stations); VOD-VI: >0.5 (n = 40 stations). The central mark within each box shows the median value, and the bottom and top edges mark the extent of the 25th and 75th percentiles. Whiskers include 99.3% of all data, corresponding approximately to ±2.7 σ. (For interpretation of the references to colour in this figure legend, the reader is referred to the web version of this article.)

0.66 to 0.68 (Table 5). The global results show contrasted results when considering different land covers: even if V2 had better scores for almost all land covers and for both the correlation and ubRMSE metrics (Fig. S4, Tables 4 & 5), the improved scores of V2 were particularly noticeable over woody vegetation (ENF, EBF, … Woody Savanna) and relatively smaller over short and sparse vegetation areas (Shrublands, Grasslands, Croplands). In terms of bias, which was considered, as noted above, as a second-order performance criterion in SMOS-IC, results of V105 and V2 are very close and SMOS-IC shows a dry bias of ~0.1 m^3/m^3 against ERA5-Land SM and of ~ −0.045 m^3/m^3 against ISMN *in situ* sites for both V2 and V105 (Tables 4 & 5). To have a better overview of the evaluation results in terms of spatial patterns we used ERA5 Land SM as a reference (Fig. S5, S6). SMOS-IC V2 is closer to the reference ERA5-Land SM data in terms of both correlation and ubRMSE over most of the pixels at global scale and in particular in forested areas in the tropical regions (Congo and Amazon basins) and northernmost regions of America and Russia. SMOS-IC V105 is closer to the reference ERA5-Land SM data mostly for the ubRMSE metric in southern China.

The impact of vegetation on the SM retrieval accuracy was evaluated using L-VOD as a parameter of vegetation density: L-VOD is directly related to the microwave extinction effects within the vegetation layer. Considering the correlation (R) metric, it is found V2 SM retrievals have a relatively low sensitivity to vegetation effects. A higher sensitivity is found for the ubRMSE metric which increases slowly for increasing L-VOD values (Fig. 2). Considering both the R and ubRMSE metrics, it is found V105 SM is more sensitive to vegetation effects than V2 SM. In particular, we can note the improvement (*i.e.* results closer to reference *in situ* data set than V105) obtained with V2 increases regularly for increasing L-VOD values (Fig. 3). These results are in good agreement with above results obtained for woody vegetation (Tables 4 and 5, Fig. S4, S5, S6) and with results using LAI, instead of L-VOD, as a proxy of vegetation density (Fig. S7, S8).

4.2.2. L-VOD

The spatial patterns of the temporal correlation between L-VOD and NDVI are relatively similar for V2 and V105 (Fig. 4). Positive correlations are generally found globally but negative correlations can be noted, especially in the tropics, including a very negative signature in the tropical forest of the Miombo (Tian et al., 2018), in southern, northern and central Europe and in the northwestern regions of the USA. In regions where correlation was positive, higher correlation values were generally obtained with V2 to the noticeable exception of the boreal regions in northeastern Russia and in Alaska (Fig. 4). The correlation increased over all land cover types which are not exclusively forest types (Table 6). Considering woody vegetation, correlation decreased slightly for categories DNF (Deciduous Needleleaf Forests), in link with the decreased correlation noted in eastern Russia, EBF (Evergreen Broadleaf Forests) and WS (Woody Savannas). But as noted before, spatial and temporal correlation between L-VOD and NDVI are not accurate criteria of the L-VOD quality over woody vegetation types as leaf development and plant water storage are not synchronous in many forest ecosystems (Tian et al., 2018; Jones et al., 2014). For instance, in regions where correlation was negative, more negative correlation values were generally obtained with V2, as in the dry tropical forests of Miombo (green area south of the Congo basin in Fig. 5), where plant water storage and leaf development are decoupled with a ~ 6 month lag (*Cf* section 5; Tian et al., 2018). The same caution in interpreting correlation values between L-VOD and NDVI can be

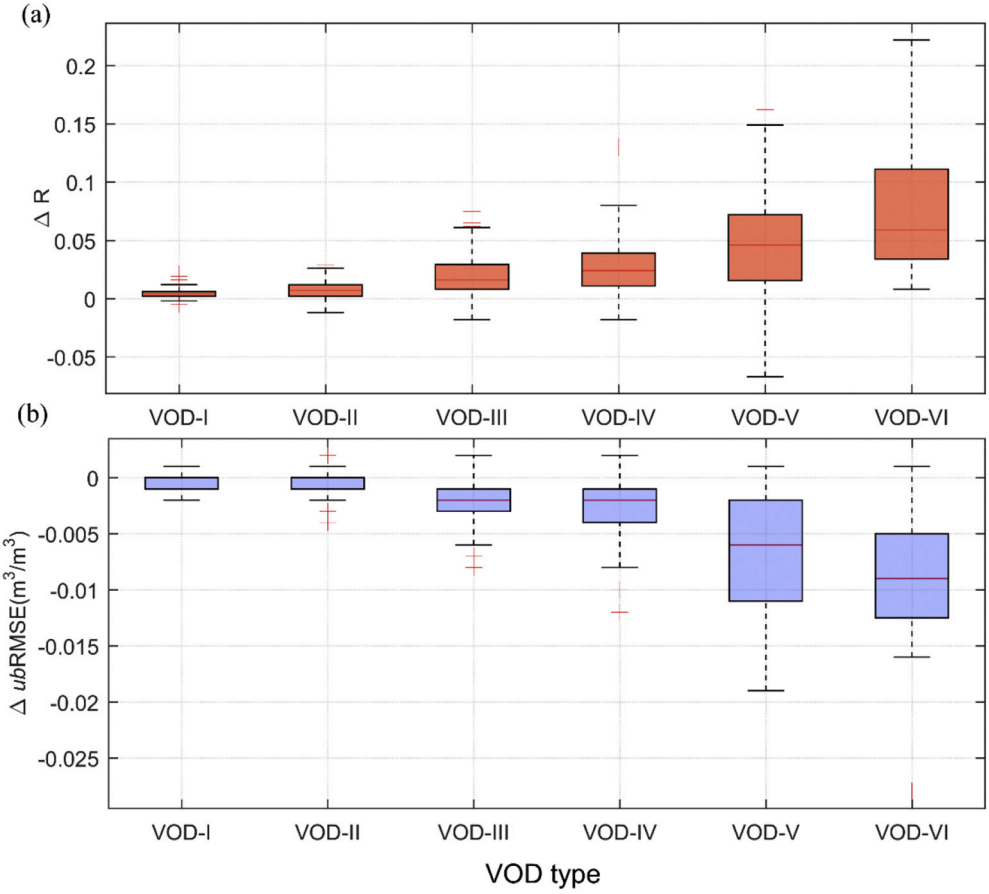

Fig. 3. idem as Fig. 2 but we computed here the differences in correlation (red) and ubRMSE (blue) for the relationship between SMOS-IC V105 SM *vs in situ* SM and V2 SM *vs in situ* SM (2014–2017) for different L-VOD intervals (*Cf* caption of Fig. 2). Note: differences between the two versions of SMOS-IC are statistically significant ($p < 0.05$, one-way ANOVA test) for all classes of R and ubRMSE.

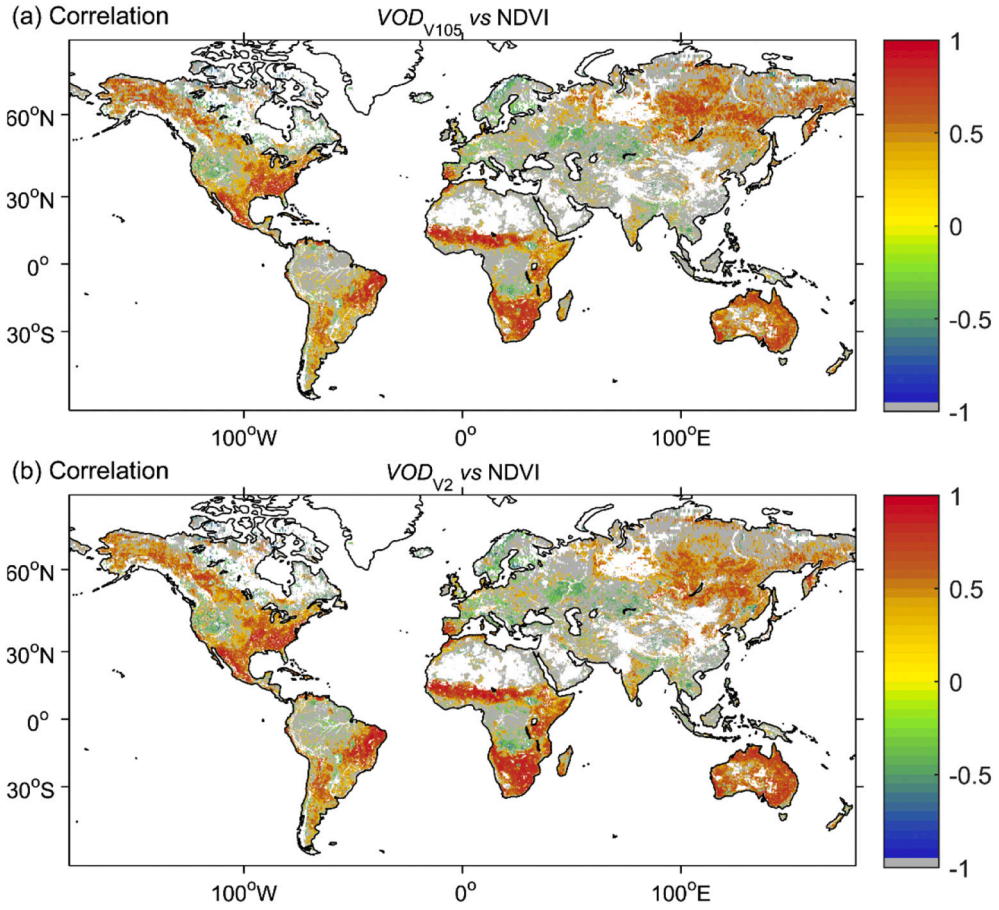

Fig. 4. Correlation coefficient of the temporal relationship between L-VOD and NDVI for (a) SMOS-IC V105 and (b) SMOS-IC V2. Blank areas correspond to pixels filtered out with the scene flags (*Cf* Table 3) and to deserts; grey areas to pixels where the correlation is not significant (non-significance was defined here by a *p*-value >0.05).

Table 6
Correlation coefficient of the temporal relationship between L-VOD and NDVI for SMOS-IC V105 and SMOS-IC V2 (2014–2017) for different vegetation types, as defined by the IGBP land cover classification.

Version	ENF	EBF	DNF	DBF	MF	SH	WS	S	G	C	CNVM	BSV	Overall
V2	0.35	0.21	0.52	0.52	0.47	0.53	0.43	0.67	0.46	0.42	0.52	0.35	0.49
V105	0.33	0.24	0.57	0.50	0.43	0.50	0.45	0.60	0.40	0.40	0.49	0.33	0.46

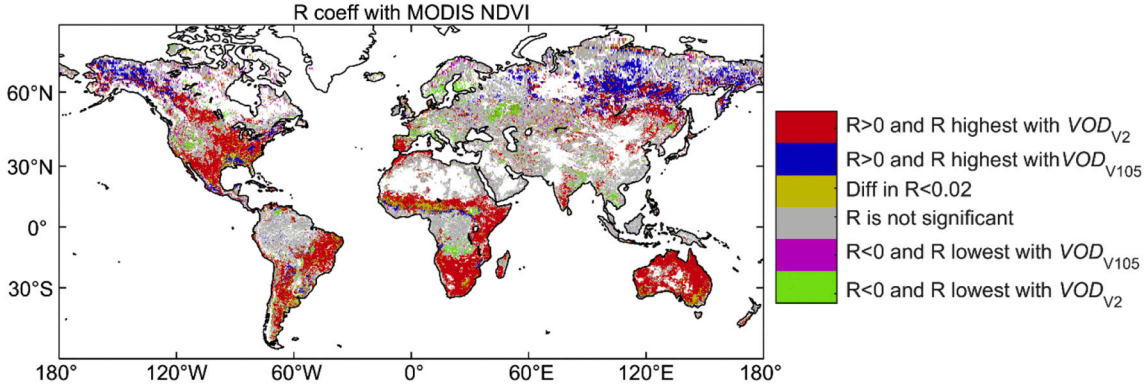

Fig. 5. Global map showing where the SMOS-IC V105 or SMOS-IC V2 L-VOD product provides the stronger temporal correlation (positive or negative) with MODIS NDVI. Pixels where the correlation is not significant (p-value >0.05, grey) or where the difference in correlation for V105 and V2 is less than 0.02 (yellow-green) are shown. Blank areas correspond to pixels filtered out with the scene flags and to deserts. (For interpretation of the references to colour in this figure legend, the reader is referred to the web version of this article.)

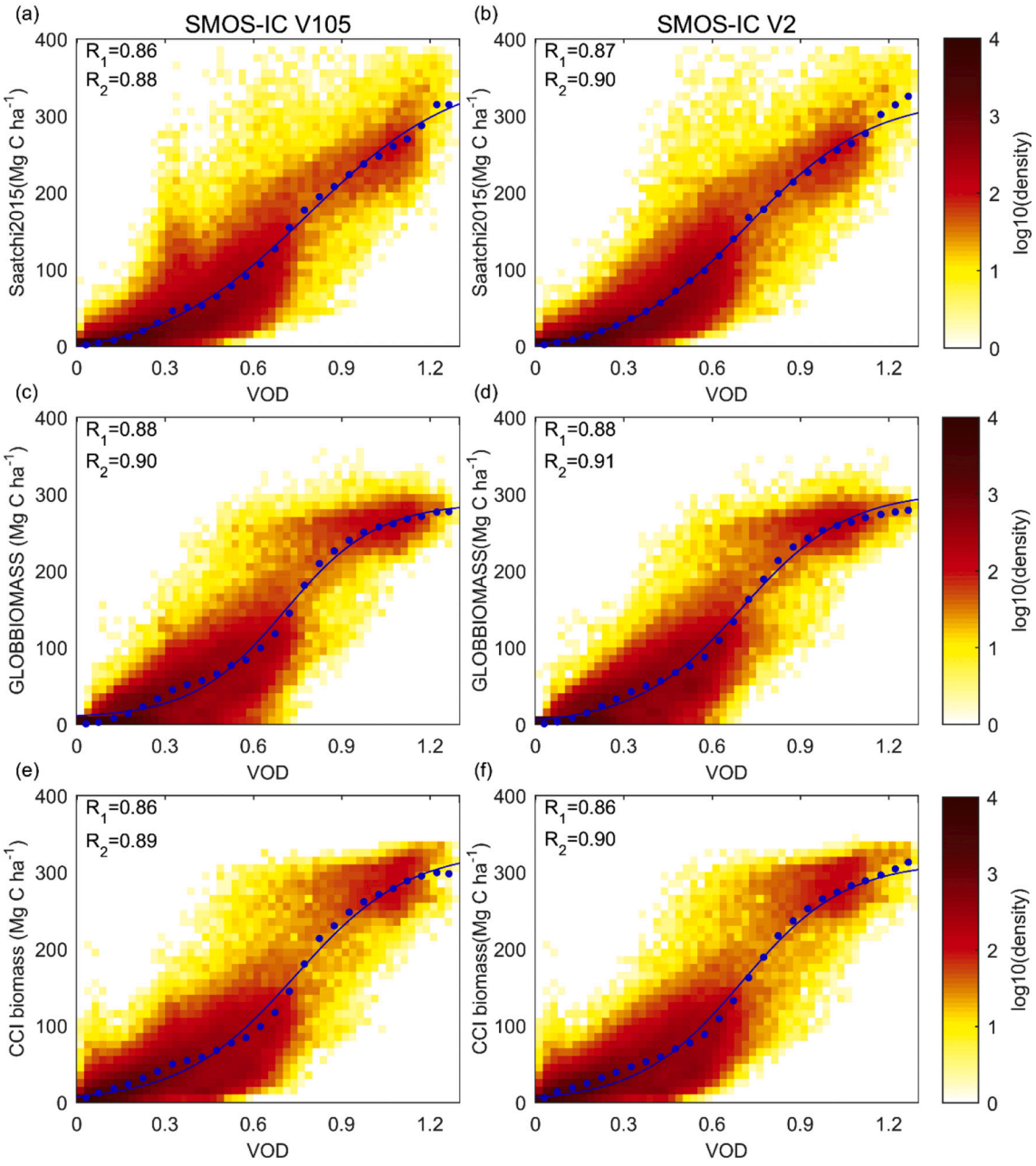

Fig. 6. Density plot of the spatial relationship between L-VOD and AGB, considering (left) L-VOD V105 and (right) L-VOD V2 and (top panel) Saatchi AGB, (middle panel) Globbiomass AGB and (bottom panel) CCI AGB. Bin-averaged L-VOD values (blue points) are fitted using a logistic function, which provided here a better fit to the data than a linear fit and are defined in Rodriguez-Fernández et al. (2018) (Table S6). R_1 is the spatial correlation coefficient computed between L-VOD and reference AGB, while R_2 is that between L-VOD-predicted AGB using the fitted logistic function and reference AGB. (For interpretation of the references to colour in this figure legend, the reader is referred to the web version of this article.)

Table 7
Correlation coefficient (R) of the spatial relationship between L-VOD for V105 and V2 against Saatchi, Globbiomass and CCI reference AGB maps (2014–2017).

	Version	ENF	EBF	DNF	DBF	MF	SH	WS	S	G	C	CNVM	BSV	Overall
Saatchi	V2	0.44	0.72	0.63	0.43	0.35	0.74	0.57	0.58	0.66	0.67	0.67	0.39	0.87
	V105	0.39	0.70	0.67	0.40	0.19	0.75	0.51	0.59	0.64	0.60	0.66	0.38	0.86
Globbiomass	V2	0.52	0.75	0.59	0.59	0.30	0.69	0.46	0.67	0.64	0.55	0.68	0.09	0.88
	V105	0.48	0.77	0.58	0.57	0.43	0.68	0.49	0.68	0.64	0.57	0.69	0.09	0.88
CCI	V2	0.47	0.75	0.45	0.44	0.28	0.38	0.37	0.62	0.72	0.46	0.62	0.40	0.86
	V105	0.43	0.76	0.44	0.42	0.36	0.38	0.36	0.62	0.71	0.49	0.63	0.40	0.86

extended to low vegetation ecosystems, considering the two L-VOD and NDVI indices are sensitive to very different vegetation features.

Considering spatial correlations, the spatial relationships computed for V105 and V2 between yearly averages of L-VOD and NDVI are very similar (Fig. S9).

The spatial correlations between average L-VOD and biomass estimated from three reference AGB maps (Saatchi, Globbbiomas and CCI) were found to be very close globally for both V105 (R ~ 0.87) and V2 (R ~ 0.88) (Fig. 6, Table 7). However, the correlation increased generally for all forest types (ENF, EBF, DBF, MF and WS) and all three reference AGB maps, except for Deciduous Needleleaf Forest (DNF) (Table 7). As noted before, this latter land cover type is mainly represented in boreal regions of northeastern Russia and this specific issue will be analyzed more in depth in the Discussion.

As illustrated over two tropical forest sites in the Congo and Amazon basins (Fig. 7), we found large differences between the time variations in L-VOD for V2 and V105, particularly in terms of high frequency variations: the time variations in L-VOD are visually found to be much smoother for V2. This can be interpreted as directly resulting from the constraint added in Eq. (2) that penalizes large VOD changes since the last VOD observations. To a lesser extent, there are also differences in terms of amplitudes and seasonal changes: the timing in the seasonal increase and decrease of L-VOD is slightly different for both L-VOD products. We attempted to quantify the change in the high frequency variations of L-VOD by mapping the standard deviation (SD_{HF}) of L-VOD for both V105 & V2 versions after removing the seasonal trend in L-VOD (Fig. 8); SD_{HF} corresponding to an estimate of the high-frequency variability in the L-VOD time series. This high-frequency variability decreased strongly with V2, particularly in the dense forests of the tropical and boreal areas (Fig. 8, Fig. S10) where SD_{HF} is generally lower than 0.02. The areas with relatively large SD_{HF} values (~0.05–0.08; corresponding to yellow-orange values in Fig. 8b) correspond to areas affected by RFI as presented in Fig. 1.

5. Review of applications

Since 2017, the use of the SMOS-IC products has been considered in several studies aiming at applications in the fields of ecology, hydrology and carbon cycle. We review some of the main achievements based on the SMOS-IC product in the following summary. All the results presented here are based on the version V105 as ongoing studies based on the version 2 have not been published yet. These results were based on both the L-VOD and SM data sets, but L-VOD played a more dominant role than SM. This can be explained by the fact that SM can be estimated globally with a good accuracy from many modelled and remotely sensed products (Al-Yaari et al., 2019a; Dong et al., 2020; Ma et al., 2019).

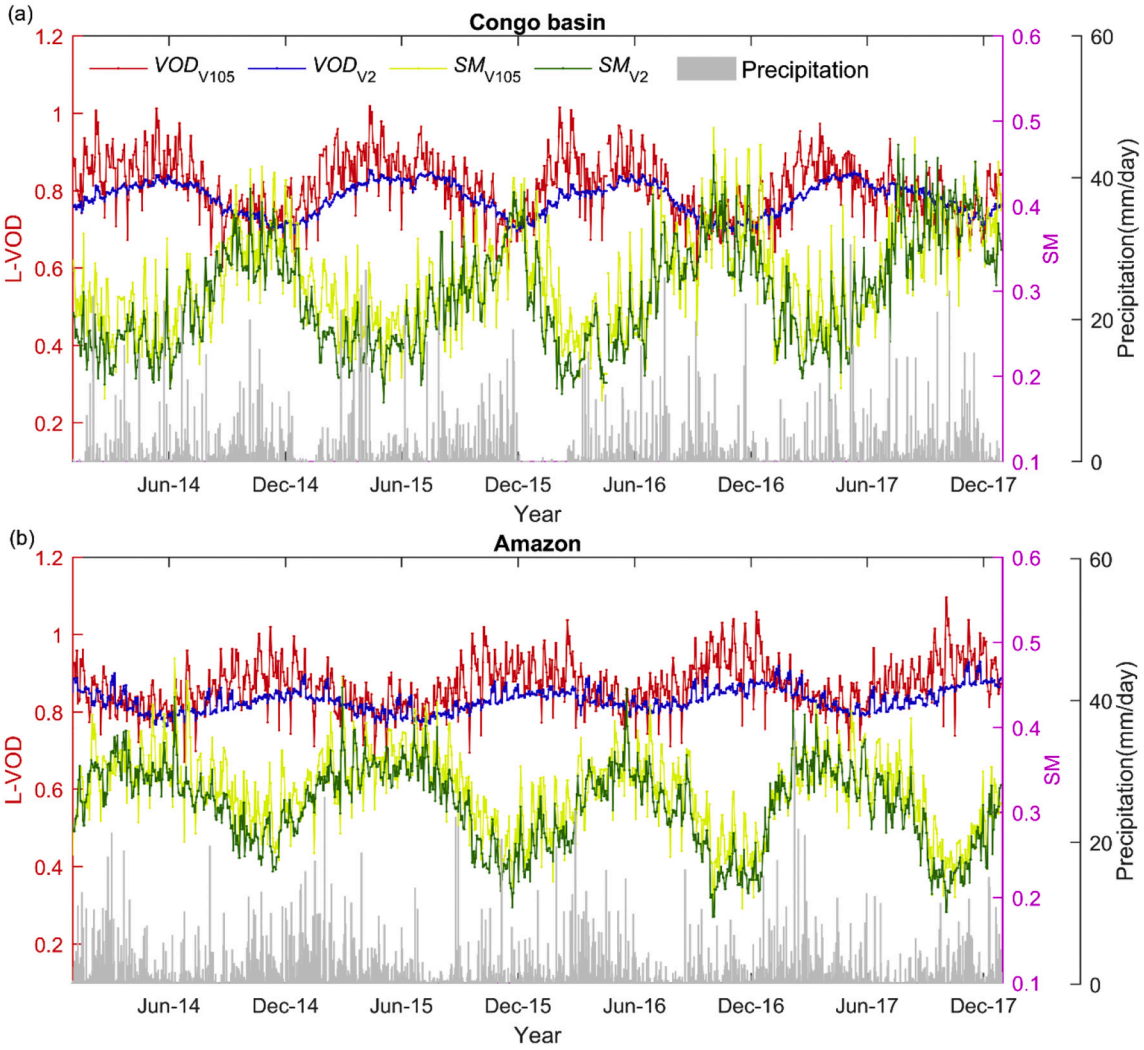

Fig. 7. L-VOD (7-day moving average) and SM time series for SMOS-IC V2 and V105 over two dense forest areas in a) the Congo basin and b) the Amazon basin. The sites cover around 16 pixels (100 km × 100 km) each, centered on (1.962°N, 18.415°E) for Congo and (−4.713°S, −63.545°W) for Amazon. The Landcover type is Evergreen Broadleaf Forest (EBF). Precipitation is shown by grey vertical bars.

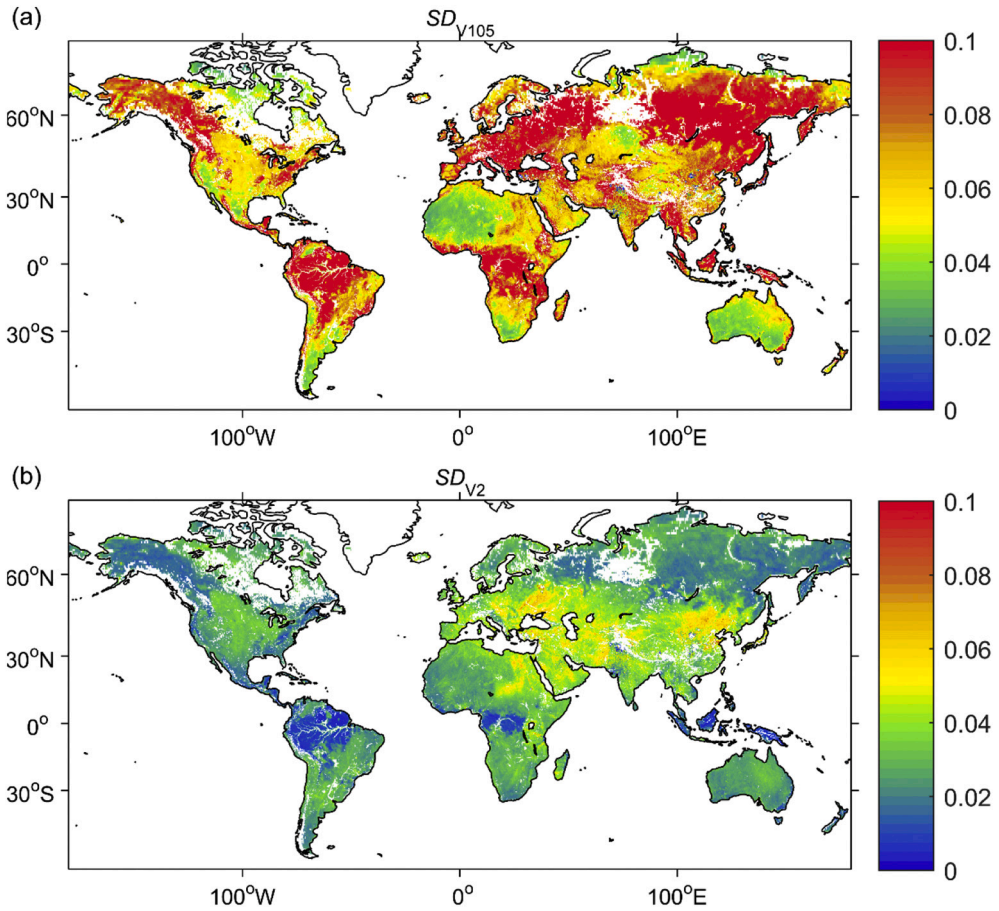

Fig. 8. Map of the standard deviation of the high-frequency variations (SD_{HF}) in the L-VOD time series for versions (a) V105 and (b) V2; the high-frequency variations in L-VOD were computed after removing the seasonal trend that was estimated with a moving average filter (period = 30 days); a map of the differences between the SD_{HF} values obtained for V105 and V2 is given in Fig. S10.

Conversely, the SMOS-IC vegetation product (L-VOD) could more easily lead to innovative results as L-VOD is a good proxy of vegetation variables, such as leaf phenology, vegetation water content, yearly average biomass, *etc.* whose dynamics are more difficult to measure in the field and to simulate with a high accuracy with current land surface models at the global scale.

As discussed above, based on a spatial calibration (as shown in Fig. S3), the SMOS-IC L-VOD product can be used to monitor the interannual variations in the aboveground carbon stocks at continental scales. The latter capabilities, showing no sign of saturation effects at high biomass levels, allowed monitoring the changes in the AGC stocks in tropical regions. A pioneer work was carried out by Brandt et al. (2018a) who revealed the applicability of L-VOD to monitor and map the yearly time changes in carbon losses and gains associated with drying trends in sub-Saharan Africa between 2010 and 2016. The trend of the net changes of AGC in drylands (53% of the land area) was -0.05 Pg C yr^{-1}, reflecting the importance of the highly dynamic and vulnerable carbon pool of dryland savannahs for the global carbon balance, despite their relatively low carbon stock per unit area. This analysis was recently extended to the whole tropics by Fan et al. (2019) who confirmed for the first time from large-scale continuous Earth Observation (EO) that the tropical net AGC budget was approximately neutral. The large interannual and spatial fluctuations of tropical AGC, quantified during the wet 2011 La Niña and the extreme dry and warm 2015–2016 El Niño episodes, were shown to be closely related to independent global atmospheric CO_2 growth-rate anomalies highlighting the pivotal role of tropical AGC in the global carbon budget. Following the 2015–2016 El Niño episode, the AGC stocks of the tropical forests were expected to partly recover. The L-VOD-based estimates of AGC, showed that the recovery of the tropical ecosystems was slow and that by the end of 2017, AGC had not reached pre-drought levels of 2014: from 2014 to 2017 tropical AGC stocks decreased by 1.3 Pg.C (Wigneron et al., 2020). Persistent AGC losses in Africa, mainly in humid forests, represented almost 70% of these losses which could be related to both deforestation and to a massive cumulative soil moisture depletion at the end of 2016, as a result of the combined El Niño anomaly and of a pre-existing drought.

In parallel to these studies focused on yearly AGC changes, the L-VOD product was applied to monitor the seasonal variations in the vegetation water content (VWC) at continental scales. Tian et al. (2018) have analyzed the coupling between L-VOD, a proxy of plant water storage (*e.g.* VWC), and leaf phenology (LAI) at global scale. The study revealed that the seasonal variations in L-VOD and LAI are highly asynchronous in dry tropical forests, where an increase in plant water storage precedes vegetation greening by ~25 to 180 days. In particular, a very intriguing signature was found in the Miombo region, an immense surface area south of the African rainforests where LAI increases several weeks before the rainy season begins (so called pre-rain green-up). In this forest area, the seasonal changes in L-VOD and LAI are asynchronous by almost 6 months: trees in Miombo takes up water at the end of the rainy season (when transpiration losses fall) and stores it in woody tissues during most of the dry season in support to the emergence of new leaves a few weeks before rain starts. This specific hydraulic behavior had previously been revealed from *in situ* experiments in dry tropical forests, particularly in Costa Rica (Borchert, 1994). The L-VOD data allowed demonstrating that this behavior is a large-scale phenomenon which extends over very large forested areas in the Miombo woodlands,

the northern African woodlands and the Brazilian Cerrado.

So far, most of the important findings based on L-VOD were obtained in the tropics. There are several explanations to this fact: (i) L-VOD is little affected by the strong limitations (cloud coverage, saturation *vs* biomass, *etc.*) affecting the optical sensors in the tropics and can thus bring a new insight over the tropical vegetation ecosystems (ii) Tropical vegetation has a pivotal role in the global carbon budget (iii) RFI has generally a weak impact on the SMOS observations in the tropical American and African continents. Yet, L-VOD is potentially a very interesting index in other regions of the world and it is currently used in several ongoing applications which could not be included in this review. These ongoing studies concern in particular Australia, where RFI is very low and L-VOD is performing very well to monitor the impact of droughts and fires on the AGC stocks and the high latitudes, where optical observations indicate widespread greening, but numerous questions and uncertainties about the vegetation change remain in those regions (Myers-Smith et al., 2018a). To complete this section, we list the SMOS IC applications in a non-exhaustive fashion in Table 8.

6. Discussion

The L-VOD products computed from the SMOS and SMAP observations are increasingly used to evaluate the link between the changing environmental conditions and vegetation functioning. In comparison to SMAP which was launched beginning of 2015, the SMOS L-VOD data set presents the advantage of being available since 2010, allowing to analyze longer trends in both soil moisture and vegetation carbon stocks. Conversely, SMAP which includes more recent technological developments, presents the advantage of being less sensitive to RFI effects which strongly affect the SMOS observations, particularly in Europe, northern Africa and many regions of Asia.

SMOS has multi-angular capabilities allowing daily simultaneous retrievals of SM and L-VOD. These capabilities were used in the first-released version of SMOS-IC (Fernandez-Moran et al., 2017a), while multi-temporal retrieval approaches have been developed for accurate SMAP L-VOD retrievals (Konings et al., 2017a). The new version (V2) of SMOS-IC which is presented in this study combines both a multi-angular and a multi-temporal retrieval approach. This combined approach led to better scores in the SM and L-VOD products considering a series of criteria for both the SM and L-VOD data:

- Considering retrieved SM data: when changing from V105 to V2, better scores were obtained in terms of both correlation (R) and ubRMSE criteria for all IGBP vegetation types, considering both *in situ* ISMN and ERA5-Land modelled data sets as a reference for comparison. For instance, considering ERA5-Land as a reference, better scores in terms of correlation and ubRMSE were obtained with SMOS-IC V2 over most (> 90%) of the pixels at global scale. Considering all ISMN *in situ* sites, the average ubRMSE decreased from 0.062 m^3/m^3 to 0.059 m^3/m^3, and median correlation (R) increased from 0.66 to 0.68 (Table 5). Using both ERA5-Land and ISMN SM data sets as references, the improved scores of V2 were larger over woody vegetation and smaller over short and sparse vegetation areas. The dry bias noted in SMOS-IC V105 remained almost constant (~ -0.045 m^3/m^3 *vs* ISMN).

- Considering retrieved L-VOD data: it should be noted that, contrary to SM, no direct estimates of L-VOD are available from measurements or models, so that only indirect evaluations based on proxies (some proxies are more relevant for short and sparse vegetation, others for forests) can be made. These limitations being noted, we found that, consistently, when upgrading from V105 to V2, better scores were obtained considering all used proxies/criteria: the spatial and temporal correlation between L-VOD/NDVI increased particularly over short vegetation areas (where the criterion is more relevant) and the spatial correlation with AGC stocks increased over woody vegetation covers (where the criterion is more relevant). Through the use of constraints (Eq. (2)), the V2 time series presented much smoother time variations than those of V105, particularly over dense forests in the tropics. Only one main limitation of V2 could be noted: lower performances were found in some boreal regions, mostly in northeastern Russia, where (i) a lower temporal correlation was found between L-VOD and NDVI (ii) a lower spatial correlation was found between L-VOD and AGB for DNF (deciduous needleleaf forest).

The improved scores of V2 SM could be noted particularly over woody land covers. A possible interpretation of this result is the following one: the main change considered in V2 was improving the L-VOD initialization in the cost function (Eqs. 1 & 2). This change affecting L-VOD will have a larger impact for woody land covers which correspond to denser vegetation canopies and higher biomass levels. So, improving the L-VOD retrievals should have a larger impact on the accuracy of the SM retrievals for those dense vegetation types which have larger extinction properties of the microwave radiations.

One exception to the improved score obtained with V2 could be noted for L-VOD retrievals in Russia. It is likely that the slight decrease in the performance of V2 *vs* V105, can be related to the specific environmental conditions prevailing in the boreal regions. In these northern regions, due to frozen conditions, the L-VOD retrievals cannot be done in winter. So, the computation of the first guess of L-VOD (*e.g.* $L\text{-}VOD^{ini}$ in Eq. (2)) has to be interrupted each year making the V2 multi-temporal retrieval approach less continuous and thus less efficient. Moreover, in V2 we used the same soil and vegetation model parameters as in V105. It is likely that the changes made in V2 could impact these model

Table 8
Overview (non-exhaustive) of scientific studies using the SMOS-IC SM or L-VOD or both SM & L-VOD data (Both) in application studies.

Region/ continent	Reference	Focus:	Main topic of the study
Africa	Brandt et al. (2018a)	Both	Carbon losses in African drylands (2010–2016)
	Rodriguez-Fernández et al. (2018)	L-VOD	Sensitivity of L-VOD to above-ground biomass
Africa Drylands	Bernardino et al. (2020)	Both	Woody plant die-off in the western Sahel
	Brandt et al. (2019)	Both	Herbaceous/woody foliage production in the Sahel
Boreal	Tagesson et al. (2020)	L-VOD	Divergence in the carbon sink of tropical and boreal forests
China	Brandt et al. (2018b)	Both	Greening and biomass increase in South China Karst during recent decade
	Tong et al. (2020)	Both	Carbon sequestration from forest management
Europe	Al-Yaari et al. (2018)	Both	Time series of SM and L-VOD at the FR-AQUI site
	Bastos et al. (2020)	Both	Legacy effects of the 2018 drought on ecosystem productivity
	Scholze et al. (2019)	Both	Mean European Carbon Sink over 2010–2015
Global	Ebrahimi-Khusfi et al. (2018)	Both	SMOS/SMAP Synergy
	Frappart et al. (2020)	L-VOD	Review
	Li et al. (in press)	L-VOD	VOD Product Inter-comparison
	Tian et al. (2018)	Both	Coupling between plant water storage and leaf phenology
Tropics	Bastos et al. (2018)	Both	Impact of the 2015–16 El Nino on the terrestrial carbon cycle
	Fan et al. (2020)	Both	Pantropical carbon dynamics (2010–2017)
	Wigneron et al. (2020)	Both	Recovery of tropical forests from the 2015–2016 El Niño event
USA	Al-Yaari et al. (2020)	Both	Asymmetric responses of ecosystem productivity
	Al-Yaari et al. (2019b)	SM	Temperature biases in CMIP5 simulations over conterminous United States
	Dong et al. (2020)	SM	Soil moisture climatology

parameters. But these changes have not been accounted for and the impact could be larger in boreal regions considering the specific environmental conditions prevailing there and in particular: (1) a large soil organic matter (SOM) which affects the soil dielectric properties in the upper soil layers (Mironov and Savin, 2015; Bircher et al., 2016); accounting for this effect in L-MEB will require the use of an accurate and global SOM map (2) land cover types with specific vegetation structure and phenology features, as can be found in particular in deciduous needleleaf forests (more than 90% of the cover fraction of this IGBP class can be found in eastern Russia) which would require performing a specific calibration of the effective scattering albedo (ω); the current L-MEB calibration of ω being only based on observations over dense tropical forests (Parrens et al., 2017).

An intriguing signature common to both V105 and V2 could be noted: the temporal correlation between L-VOD and both NDVI and SM is low in some regions of the tropics and particularly in the Amazon and Congo basins (Figs. 4 & 7). The validity of this result cannot be clearly evaluated as very few *in situ* data sets are available in these tropical regions to carry out an accurate evaluation of the SM and L-VOD products. It could be due to an artefact in the retrieval process in these regions with very dense vegetation covers. But many questions are still open on that topic in the Amazon basin. For instance, relatively large time lags (~3 months in some regions and following a gradient from West to East) have been found between different climate variables (SM, rainfalls, Photosynthetically active radiation) and vegetation indices (NDVI and VOD) (Jones et al., 2014; Tian et al., 2018). Note that this time lag was also found considering the SMAP SM retrievals which correlate very well with the SMOS-IC SM data in the Amazon basin (M. Sadeghi, personal communications).

7. Conclusions and perspectives

Higher scores were obtained with SMOS-IC V2 *vs* the previous V105 version considering several criteria for both SM and L-VOD. Moreover, the algorithmic changes made in Eq. (2) might result in more stable retrievals which is reflected in particular by more stable time variations in L-VOD. This should be very beneficial for the different application topics that we reviewed in this study. The analysis of the V2 results made in the previous sections clearly opened new fields of investigations and perspectives:

-Improving RFI filtering. To avoid very erroneous results, the RFI effects which contaminate the SMOS-IC time series should be filtered very carefully. This is particularly true for L-VOD which is more sensitive to RFI effects than SM. So, currently, the difficulty in applying automatic multi-annual and global RFI filtering still strongly limits the potential applications of SMOS-IC. Such automatic filters are being evaluated for the next SMOS-IC versions.

-Improving L-VOD retrievals in boreal regions, particularly in eastern Russia. The key and specific features to consider in these regions include: (i) the large fraction of soil organic matter (SOM) (ii) the vegetation structure and phenological features of deciduous needleleaf forests and (iii) the soil frozen conditions which affect the multi-temporal retrieval continuity.

-Evaluating a new calibration of the soil and model parameters in SMOS-IC, considering the combined multi-temporal and multi-angular retrieval approach developed in V2. In particular, all recent inter-comparison studies showed that the retrieved SMOS-IC SM values were affected by a negative bias, which is higher than that of most products, including SMOS L2 and L3 (Al-Yaari et al., 2019a; Dong et al., 2020; Ma et al., 2019; Quets et al., 2019). Even though reducing the bias in retrieved SM was considered as a second order priority, as compared to the correlation and ubRMSE metrics, the SMOS-IC SM bias may affect the L-VOD retrievals. Future activities will consider reducing this SM bias by improving parameter calibration and ancillary data inputs such as surface temperature as suggested by Ma et al. (2019). Evaluating more in depth the seasonal variations in both SM and L-VOD in the tropical regions and particularly in the Amazon and Congo basins, which are key regions of application of the SMOS-IC product (Brandt et al., 2018a; Fan et al., 2019; Wigneron et al., 2020). The evaluation should in particular consider the time lag found between the SMOS-IC SM, L-VOD and MODIS NDVI (Tian et al., 2018).

Beyond the results of the present evaluation of V2, the review of the SMOS-IC application studies in link with climate change and increased mortality risks in forests (*Cf* section 5) showed the key interest of long-term SM and L-VOD times series. ESA CCI and other remotely-sensed and modelled products provide long time series of soil moisture. However, no passive microwave satellite at L-band was available before the SMOS launch (end of Nov. 2009) and, to our knowledge, all L-VOD time series begin in 2010 with SMOS. To extend the L-VOD time series in the past, before 2010, merging method with VOD products derived from other sensors such as the Advanced Microwave Scanning Radiometer—EOS (AMSR-E) can be used (Jones et al., 2014). To our knowledge, this is not done already. Continuity in the future should also be considered. Some passive microwave space-borne missions including L-band have been investigated in China (Water Cycle Observation Mission (WCOM); Shi et al., 2016) and are still under evaluation in Europe (Copernicus Imaging Microwave Radiometer (CIMR); Kilic et al., 2018), but no decision has been taken to date by any Space Agencies. So, continuity in the L-VOD time series will be supported only by the SMOS and SMAP instruments in the coming years and the next step in the SMOS-IC project will be merging the SMOS and SMAP L-VOD time series, in an effort to ensure L-VOD continuity if one of the two sensors fails in the near future.

Data availability

The SMOS-IC data sets in version V2 and V105 can be available upon request to the authors. The SMOS-IC V2 SM data set is freely available at https://ib.remote-sensing.inrae.fr/

Author contribution

JPW and X. Li designed the V2 algorithm. JPW wrote the first draft of the manuscript. X. Li did the data analysis and designed the figures. All authors contributed to the discussion and revised the submitted manuscript.

Declaration of Competing Interest

The authors declare that they have no conflict of interest.

Acknowledgements

This work was supported by the SMOS project of the TOSCA Programme from CNES, France (Centre National d'Etudes Spatiales) and Xiaojun Li was sponsored by China Scholarship Council (CSC; 201804910838). The authors wish to thank the three reviewers for their detailed and constructive comments which helped us to improve considerably the manuscript.

Appendix A. Supplementary data

Supplementary data to this article can be found online at https://doi.org/10.1016/j.rse.2020.112238.

References

Al Bitar, A., Mialon, A., Kerr, Y.H., Cabot, F., Richaume, P., Jacquette, E., Quesney, A., Mahmoodi, A., Tarot, S., Parrens, M., 2017. The global SMOS level 3 daily soil moisture and brightness temperature maps. Earth Syst. Sci. Data 9, 293–315.

Albergel, C., De Rosnay, P., Balsamo, G., Isaksen, L., Muñoz-Sabater, J., 2012. Soil moisture analyses at ECMWF: evaluation using global ground-based in situ observations. J. Hydrometeorol. 13, 1442–1460.

Albergel, C., Dorigo, W., Reichle, R.H., Balsamo, G., de Rosnay, P., Muñoz-Sabater, Isaksen, de Jeu, L., Wagner, R., W., 2013. Skill and global trend analysis of soil moisture from Reanalyses and microwave remote sensing. J. Hydrometeorol. 14 (4), 1259–1277.

Al-Yaari, A., Wigneron, J.-P., Ducharne, A., Kerr, Y., De Rosnay, P., De Jeu, R., Govind, A., Al Bitar, A., Albergel, C., Munoz-Sabater, J., 2014. Global-scale evaluation of two satellite-based passive microwave soil moisture datasets (SMOS and AMSR-E) with respect to land data assimilation system estimates. Remote Sens. Environ. 149, 181–195.

Al-Yaari, A., Dayau, S., Chipeaux, C., Aluome, C., Kruszewski, A., Loustau, D., Wigneron, J.-P., 2018. The AQUI soil moisture network for satellite microwave remote sensing validation in South-Western France. Remote Sens. 10, 1839.

Al-Yaari, A., Wigneron, J.-P., Dorigo, W., Colliander, A., Pellarin, T., Hahn, S., Mialon, A., Richaume, P., Fernandez-Moran, R., Fan, L., Kerr, Y.H., De Lannoy, G., 2019a. Assessment and inter-comparison of recently developed/reprocessed microwave satellite soil moisture products using ISMN ground-based measurements. Remote Sens. Environ. 224, 289–303.

Al-Yaari, A., Ducharne, A., Cheruy, F., Crow, W.T., Wigneron, J.-P., 2019b. Satellite-based soil moisture provides missing link between summertime precipitation and surface temperature biases in CMIP5 simulations over conterminous United States. Sci. Rep. 9, 1657.

Al-Yaari, A., Wigneron, J.-P., Philippe, P., Reichstein, M., Ballantyne, A., Ogée, J., Ducharne, A., Swenson, J.J., Frappart, F., Fan, L., Wingate, L., Li, X., Hufkens, K., Knapp, A.K., 2020. Asymmetric responses of ecosystem productivity to rainfall anomalies vary inversely with mean annual rainfall over the conterminous U.S. Glob. Chang. Biol. 00, 1–15.

Bastos, A., Friedlingstein, P., Sitch, S., Chen, C., Mialon, A., Wigneron, J.-P., Arora, V.K., Briggs, P.R., Canadell, J.G., Ciais, P., Chevallier, F., Delire, C., Haverd, V., Jain, A.K., Joos, F., Kato, E., Lienert, S., Lombardozzi, D., Melton, J.R., Myneni, R., Nabel, J.E. M.S., Pongratz, J., Poulter, B., Rödenbeck, C., Séférian, R., Tian, H., van Eck, C., Viovy, N., Vuichard, N., Walker, A.P., Wiltshire, A., Yang, J., Zaehle, S., Zhu, D., 2018. Impact of the 2015-16 El Nino on the terrestrial carbon cycle constrained by bottom-up and top-down approaches. Philos. Trans. R. Soc. B 20170304.

Bastos, A., Ciais, P., Friedlingstein, P., Sitch, S., Pongratz, J., Fan, L., Wigneron, J.-P., Weber, U., Reichstein, M., Fu, Z., et al., 2020. Direct and seasonal legacy effects of the 2018 heat wave and drought on European ecosystem productivity. Sci. Adv. 6 (24), eaba2724.

Bell, J.E., Palecki, M.A., Baker, C.B., Collins, W.G., Lawrimore, J.H., Leeper, R.D., Hall, M.E., Kochendorfer, J., Meyers, T.P., Wilson, T., 2013. US Climate Reference Network soil moisture and temperature observations. J. Hydrometeorol 14, 977–988.

Bernardino, P., Brandt, M., De Keersmaecker, W., Horion, S., Fensholt, R., Storms, L., Wigneron, J.-P., Verbesselt, J., Somers, B., 2020. Uncovering dryland woody dynamics using optical, microwave, and field data: prolonged above-average rainfall surprisingly contributes to woody plant die-off in the western Sahel. Remote Sens. 12, 2332.

Bircher, S., Demontoux, F., Razafindratsima, S., Zakharova, E., Drusch, M., Wigneron, J.-P., Kerr, Y., 2016. L-band relative permittivity of organic soil surface layers – a new dataset of resonant cavity measurements and model evaluation. Remote Sens. 8, 1024.

Borchert, R., 1994. Soil and stem water storage determine phenology and distribution of tropical dry forest trees. Ecology. 75, 1437–1449.

Brando, P.M., Goetz, S.J., Baccini, A., Nepstad, D.C., Beck, P.S.A., Christman, M.C., 2010. Seasonal and interannual variability of climate and vegetation indices across the Amazon. Proc. Natl. Acad. Sci. U. S. A. 107, 14685–14690.

Brandt, M., Wigneron, J.-P., Chave, J., Tagesson, T., Penuelas, J., Ciais, P., Rasmussen, K., Tian, F., Mbow, C., Al-Yaari, A., Rodriguez-Fernandez, N., Schurgers, G., Zhang, W., Chang, J., Kerr, Y., Verger, A., Tucker, C., Mialon, A., Rasmussen, L.V., Fan, L., Fensholt, R., 2018a. Satellite passive microwaves reveal recent climate-induced carbon losses in African drylands. Nat. Ecol. Evol. 2, 827–835.

Brandt, M., Yue, Y., Wigneron, J.-P., Tong, X., Tian, F., Rudbeck Jepsen, M., Xiao, X., Verger, A., Mialon, A., Al-Yaari, A., Wang, K., Fensholt, R., 2018b. Satellite-observed major greening and biomass increase in south China karst during recent decade. Earth's Future 6.

Brandt, M., Hiernaux, P., Rasmussen, K., Tucker, C.J., Wigneron, J.-P., Diouf, A., Herrmann, S., Zhang, W., Kergoat, L., Mbow, C., Abel, C., Auda, Y., Fensholt, R., 2019. Changes in rainfall distribution promote woody foliage production in the Sahel. Commun. Biol. 2, 133.

Broxton, P.D., Zeng, X., Sulla-Menashe, D., Troch, P.A., 2014. A global land cover climatology using MODIS data. J. Appl. Meteorol. Climatol. 53, 1593–1605.

Calvet, J.-C., Fritz, N., Froissard, F., Suquia, D., Petitpa, A., Piguet, B., 2007. In situ soil moisture observations for the CAL/VAL of SMOS: the SMOSMANIA network. In: 2007 IEEE International Geoscience and Remote Sensing Symposium. IEEE, pp. In: 1196–1199.

Carreiras, J.M.B., Quegan, S., Le Toan, T., Minh, D.H., Saatchi, S.S., Carvalhais, N., Reichstein, M., Scipal, K., 2017. Coverage of high biomass forests by the ESA BIOMASS mission under defense restrictions. Remote Sens. Environ. 196, 154–162.

CCI AGB D4.3, 2020. http://cci.esa.int/sites/default/files/biomass_D4.3_Product_User_Guide_V1.0.pdf.

Chaparro, D., Duveiller, G., Piles, M., Cescatti, A., Vall-llossera, M., Camps, A., Entekhabi, D., 2019. Sensitivity of L-band vegetation optical depth to carbon stocks in tropical forests: a comparison to higher frequencies and optical indices. Remote Sens. Environ. 232, 111303.

Chaubell, M.J., Yueh, S.H., Dunbar, R.S., Colliander, A., Dunbar, R.S., Chen, F., Chan, S. K., Entekhabi, D., Bindlish, R., O'Neill, P., et al., 2020. Improved SMAP Dual-Channel algorithm for the retrieval of soil moisture. IEEE Trans. Geosci. Remote Sens. 58 (6), 3894–3905.

Colliander, A., Cosh, M.H., Misra, S., Jackson, T.J., Crow, W.T., Chan, S., Bindlish, R., Chae, C., Holifield Collins, C., Yueh, S.H., 2017. Validation and scaling of soil moisture in a semi-arid environment: SMAP validation experiment 2015 (SMAPVEX15). Remote Sens. Environ. 196, 101–112.

Crow, W.T., Wood, E.F., 2002. Impact of soil moisture aggregation on surface energy flux prediction during SGP ' 97. Geophys. Res. Lett. 29, 1–4.

De Lannoy, G.J.M., Reichle, R.H., 2016. Assimilation of SMOS brightness temperatures or soil moisture retrievals into a land surface model. Hydrol. Earth Syst. Sci. 20, 4895–4911.

Dee, D.P., Uppala, S., Simmons, A., Berrisford, P., Poli, P., Kobayashi, S., Andrae, U., Balmaseda, M., Balsamo, G., Bauer, D.P., 2011. The ERA-interim reanalysis: configuration and performance of the data assimilation system. Q. J. R. Meteorol. Soc. 137, 553–597.

Dong, J., Crow, W., Tobin, K., Cosh, M., Bosch, D., Starks, P., Seyfried, M., Collins, C.D., 2020. Comparison of microwave remote sensing and land surface modeling for surface soil moisture climatology estimation. Remote Sens. Environ. 242, 111756.

Dorigo, W., Wagner, W., Hohensinn, R., Hahn, S., Paulik, C., Xaver, A., Gruber, A., Drusch, M., Mecklenburg, S., Van Oevelen, P., Robock, A., Jackson, T.J., 2011. The international soil moisture network: a data hosting facility for global in situ soil moisture measurements. Hydrol. Earth Syst. Sci. 15, 1675–1698.

Ebrahimi-Khusfi, M., Alavipanah, S.K., Hamzeh, S., Amiraslani, F., Neysani, N.S., Wigneron, J.-P., 2018. Comparison of soil moisture retrieval algorithms based on the synergy between SMAP and SMOS-IC. Int. J. Appl. Earth Obs. Geoinf. 67, 148–160.

Entekhabi, D., Njoku, E.G., O'Neill, P.E., Kellogg, K.H., Crow, W.T., Edelstein, W.N., Entin, J.K., Goodman, S.D., Jackson, T.J., Johnson, J., Kimball, J., Piepmeier, J.R., Koster, R.D., Martin, N., McDonald, K.C., Moghaddam, M., Moran, S., Reichle, R., Shi, J.C., Spencer, M.W., Thurman, S.W., Tsang, L., Van Zyl, J., 2010. The soil moisture active passive (SMAP) mission. Proc. IEEE 98, 704–716.

Fan, L., Wigneron, J.-P., Ciais, P., Chave, J., Brandt, M., Fensholt, R., Saatchi, S.S., Bastos, A., Al-Yaari, A., Hufkens, K., Qin, Y., Xiao, X., Chen, C., Myneni, R.B., Fernandez-Moran, R., Mialon, A., Rodriguez-Fernandez, N.J., Kerr, Y., Tian, F., Penuelas, J., 2019. Satellite observed pantropical carbon dynamics. Nat. Plants. 5, 944–951.

Fan, X., Liu, Y., Gan, G., Wu, G., 2020. SMAP underestimates soil moisture in vegetation-disturbed areas primarily as a result of biased surface temperature data. Remote Sens. Environ. 247, 111914.

Feldman, A.F., Short Gianotti, D.J., Konings, A.G., McColl, K.A., Akbar, R., Salvucci, G. D., Entekhabi, D., 2018. Moisture pulse-reserve in the soil-plant continuum observed across biomes. Nat. Plants 4, 1026–1033.

Fernandez-Moran, R., Wigneron, J.-P., De Lannoy, G., Lopez-Baeza, E., Parrens, M., Mialon, A., Mahmoodi, A., Al-Yaari, A., Bircher, S., Al Bitar, A., Richaume, P., Kerr, Y., 2017a. A new calibration of the effective scattering albedo and soil roughness parameters in the SMOS SM retrieval algorithm. Int. J. Appl. Earth Obs. Geoinf. 62, 27–38.

Fernandez-Moran, R., Al-Yaari, A., Mialon, A., Mahmoodi, A., Al Bitar, A., De Lannoy, G., Rodriguez-Fernandez, N., Lopez-Baeza, E., Kerr, Y., Wigneron, J.-P., 2017b. SMOS-IC: an alternative SMOS soil moisture and vegetation optical depth product. Remote Sens. 9, 457.

Ferrazzoli, P., Guerriero, L., Wigneron, J.-P., 2002. Simulating L-band emission of forests in view of future satellite applications. IEEE Trans. Geosc. Remote Sens. 40 (12), 2700–2708.

Frappart, F., Wigneron, J.-P., Li, X., Liu, X., Al-Yaari, A., Fan, L., Wang, M., Moisy, C., Le Masson, E., Aoulad Lafikh, Z., Valle, C., Ygorra, B., Baghdadi, N., 2020. Global monitoring of the vegetation dynamics from the vegetation optical depth (VOD): a review. Remote Sens. 12, 2915.

Grant, J.P., Wigneron, J.-P., De Jeu, R.A.M., Lawrence, H., Mialon, A., Richaume, P., Al Bitar, A., Drusch, M., Van Marle, M.J.E., Kerr, Y., 2016. Comparison of SMOS and AMSR-E vegetation optical depth to four MODIS-based vegetation indices. Remote Sens. Environ. 172, 87–100.

Gruber, A., De Lannoy, G., Albergel, C., Al-Yaari, A., Brocca, L., Calvet, J.-C., Colliander, A., Cosh, M., Crow, W., Dorigo, W., Draper, C., Hirschi, M., Kerr, Y., Konings, A., Lahoz, W., Coll, K. Mc, Montzka, C., Muñoz-Sabater, J., Peng, J., Reichle, R., Richaume, P., Rüdiger, C., Scanlon, T., van der Schalie, R., Wigneron, J.-P., Wagner, W., 2020. Validation practices for satellite soil moisture retrievals: what are (the) errors? Remote Sens. Environ. 244, 111806.

Hersbach, H., Bell, B., Berrisford, P., Hirahara, S., Horányi, A., Muñoz-Sabater, J., Nicolas, J., Peubey, C., Radu, R., Schepers, D., Simmons, A., et al., 2020. The ERA5 global reanalysis. Q. J. R. Meteorol. Soc. 146, 1999–2049.

Huffman, G.J., Stocker, E.F., Bolvin, D.T., Nelkin, E.J., Jackson, T., 2019. GPM IMERG Late Precipitation L3 1 day 0.1 degree x 0.1 degree V06. NASA's Precipitation Processing Center, Greenbelt, Maryland. https://doi.org/10.5067/GPM/IMERGDL/DAY/06.

Jackson, T.J., Schmugge, T.J., 1991. Vegetation effects on the microwave emission of soils. Remote Sens. Environ. 36 (3), 203–212.

Jones, M.O., Kimball, J.S., Nemani, R.R., 2014. Asynchronous Amazon forest canopy phenology indicates adaptation to both water and light availability. Environ. Res. Lett. 9, 124021.

Kerr, Y.H., Waldteufel, P., Richaume, P., Wigneron, J.-P., Ferrazzoli, P., Mahmoodi, A., Al Bitar, A., Cabot, F., Gruhier, C., Juglea, Leroux D., Mialon, A., Delwart, S., 2012. The SMOS soil moisture retrieval algorithm. IEEE Trans. Geosc. Remote Sens. 50 (5), 1384–1403.

Kerr, Y.H., Al-Yaari, A., Rodriguez-Fernandez, N., Parrens, M., Molero, B., Leroux, D., Bircher, S., Mahmoodi, A., Mialon, A., Richaume, P., Delwart, S., Al Bitar, A., Pellarin, T., Bindlish, R., Jackson, T.J., Rudiger, C., Waldteufel, P., Mecklenburg, S.,

Wigneron, J.-P., 2016. Overview of SMOS performance in terms of global soil moisture monitoring after six years in operation. Remote Sens. Environ. 180, 40–63.
Kilic, L., Prigent, C., Aires, F., Boutin, J., Heygster, G., Tonboe, R.T., Roquet, H., Jimenez, C., Donlon, C., 2018. Expected performances of the Copernicus imaging microwave radiometer (CIMR) for an all-weather and high spatial resolution estimation of ocean and sea ice parameters. J. Geophys. Res. Oceans 123, 7564–7580.
Kim, H., Wigneron, J.-P., Kumar, S., Dong, J., Wagner, W., Cosh, M.H., Bosch, D.D., Collins, C.H., Starks, P.J., Seyfried, M., Lakshmi, V., 2020. Global scale error assessments of soil moisture estimates from microwave-based active and passive satellites and land surface models over Forest and agricultural regions. Remote Sens. Environ. 251, 112052.
Konings, A.G., Gentine, P., 2016. Global variations in ecosystemscale isohydricity. Glob. Chang. Biol. 23, 891–905.
Konings, A.G., Piles, M., Rötzer, K., McColl, K.A., Chan, S.K., Entekhabi, D., 2016. Vegetation optical depth and scattering albedo retrieval using time series of dual-polarized L-band radiometer observations. Remote Sens. Environ. 172, 178–189.
Konings, A.G., Williams, A.P., Gentine, P., 2017a. Sensitivity of grassland productivity to aridity controlled by stomatal and xylem regulation. Nat. Geosci. 10, 284–288.
Konings, A.G., Piles, M., Das, N., Entekhabi, D., 2017b. L-band vegetation optical depth and effective scattering albedo estimation from SMAP. Remote Sens. Environ. 198, 460–470.
Konings, A.G., Rao, K., Steele-Dunne, S.C., 2019. Macro to micro: microwave remote sensing of plant water content for physiology and ecology. New Phytol. 223, 1166–1172.
Larson, K.M., Small, E.E., Gutmann, E.D., Bilich, A.L., Braun, J.J., Zavorotny, V.U., 2008. Use of GPS receivers as a soil moisture network for water cycle studies. Geophys. Res. Lett. 35.
Lawrence, H., Wigneron, J.-P., Lopez-Baeza, E., Novello, N., Mialon, A., Richaume, P., Al Bitar, A., Grant, J.P., Merlin, O., Leroux, D., Bircher, S., Kerr, Y., 2014. Comparison between SMOS vegetation optical depth products and MODIS vegetation indices over the USA. Remote Sens. Environ. 140, 396–406.
Lebel, T., Cappelaere, B., Galle, S., Hanan, N., Kergoat, L., Levis, S., Vieux, B., Descroix, L., Gosset, M., Mougin, E., 2009. AMMA-CATCH studies in the Sahelian region of West-Africa: an overview. J. Hydrol. 375, 3–13.
Li, M., Wu, P., Ma, Z., 2020b. A comprehensive evaluation of soil moisture and soil temperature from third-generation atmospheric and land reanalysis data sets. Int. J. Climatol. 1–23.
Li, X., Al-Yaari, A., Schwank, M., Fan, L., Frappart, F., Swenson, J., Wigneron, J.-P., 2020a. Compared performances of SMOS-IC soil moisture and vegetation optical depth retrievals based on tau-omega and two-stream microwave emission models. Remote Sens. Environ. 236, 111502.
Li, X. Wigneron, J.-P., Frappart, F., Fan, L., Ciais, P., Fensholt, R., Entekhabi, D., Brandt, M., Konings, A. G., Liu, X., Wang, M., Al-Yaari, A., Moisy, C., Global-scale assessment and inter-comparison of recently developed/reprocessed microwave satellite vegetation optical depth products. Remote Sens. Environ., (in press), 112208, 10.1016/j.rse.2020.112208.
Liu, J. Chai, L., Dong, J., Zheng, D., Wigneron, J.-P., Liu, S., Zhou, Ji, Xu, T., Yang, S., Song, Y., Qu, Y., Lu, Z., Uncertainty analysis of eleven multisource soil moisture products in the third pole environment based on the three-corned hat method, Remote Sens. Environ., (in press).
Liu, Y.Y., Van Dijk, A.I., De Jeu, R.A., Canadell, J.G., Mc-Cabe, M.F., Evans, J.P., Wang, G., 2015. Recent reversal in loss of global terrestrial biomass. Nat. Clim. Chang. 5, 470–474.
Long, D.G., Brodzik, M.J., Hardman, M.A., 2019. Enhanced-Resolution SMAP Brightness Temperature Image Products. IEEE Trans. Geosci. Remote Sens. 57 (7), 4151–4163.
Ma, H., Zeng, J., Chen, N., Zhang, X., Cosh, H.M., Wang, W., 2019. Satellite surface soil moisture from SMAP, SMOS, AMSR2 and ESA CCI: A comprehensive assessment using global ground-based observations. Remote Sens. Environ. 231, 111215.
Mialon, A., Coret, L., Kerr, Y., Sécherre, F., Wigneron, J.-P., 2008. Flagging the topographic impact on the SMOS signal. IEEE Geosci. Remote Sens. 46 (3).
Mironov, V., Savin, I., 2015. A temperature-dependent multi-relaxation spectroscopic dielectric model for thawed and frozen organic soil at 0.05–15 GHz. Phys. Chem. Earth. Parts ABC 83–84, 57–64.
Moesinger, L., Dorigo, W., de Jeu, R., van der Schalie, R., Scanlon, T., Teubner, I., Forkel, M., 2020. The global long-term microwave vegetation optical depth climate archive (VODCA). Earth Syst. Sci. Data. 12, 177–196.
Moghaddam, M., Entekhabi, D., Goykhman, Y., Li, K., Liu, M., Mahajan, A., Nayyar, A., Shuman, D., Teneketzis, D., 2010. A wireless soil moisture smart sensor web using physics-based optimal control: concept and initial demonstrations. IEEE Journal of Selected Topics in Applied Earth Observations and Remote Sensing 3, 522–535.
Momen, M., Wood, J.D., Novick, K.A., Pangle, R., Pockman, W.T., McDowell, N.G., Konings, A.G., 2017. Interacting effects of leaf water potential and biomass on vegetation optical depth. J. Geophys. Res. Biogeosci. 122, 3031–3046.
Myers-Smith, I.H., Kerby, J.T., Phoenix, G.K., Bjerke, J.W., Epstein, H.E., Assmann, J.J., John, C., Andreu-Hayles, L., Angers-Blondin, S., Beck, P.S.A., et al., 2018. Complexity revealed in the greening of the Arctic. Nat. Clim. Chang. 10, 106–117.
O'Neill, P., Chan, S., Njoku, E., Jackson, T.J., Bindlish, R., 2018. Algorithm Theoretical Basis Document Level 2 & 3 Soil Moisture (Passive) Data Products. Rev. C. SMAP Project, JPL D-66480. Jet Propulsion Laboratory, Pasadena, CA. Available at. http://smap.jpl.nasa.gov/science/dataproducts/ATBD/.
Parrens, M., Wigneron, J.-P., Richaume, P., Mialon, A., Al Bitar, A., Fernandez-Moran, R., Al-Yaari, A., Kerr, Y.H., 2016. Global-scale surface roughness effects at L-band as estimated from SMOS observations. Remote Sens. Environ. 181, 122–136.
Parrens, M., Al Bitar, A., Mialon, A., Fernandez-Moran, R., Ferrazzoli, P., Kerr, Y., Wigneron, J.-P., 2017. Estimation of the L-band effective scattering albedo of tropical forests using SMOS observations. IEEE Geosci. Remote Sens. Lett. 14-8, 1223–1227.
Peng, J., Niesel, J., Loew, A., Zhang, S., Wang, J., 2015. Evaluation of satellite and reanalysis soil moisture products over Southwest China using ground-based measurements. Remote Sens. 7 (11), 15729–15747.
Pulliainen, J., Karna, J.-P., Hallikainen, M., 1993. Development of geophysical retrieval algorithms for the MIMR. IEEE Trans. Geosci. Remote Sens. 31 (1), 268–277.
Qin, Y., Xiao, X., Wigneron, J.-P., Ciais, P., Canadell, J.G., Brandt, M., Li, X., Fan, L., Wu, X., Tang, H., Dubayah, R., Doughty, R., Chang, Q., Crowell, S., Bo, Z., Moore III, B., 2020. Unexpected large forest fires and biomass loss in 2019 over Australia. Nat. Clim. Chang. (in review).
Quets, J., De Lannoy, G.J.M., Al Yaari, A., Chan, S., Cosh, M.H., Gruber, A., Reichle, R.H., Van der Schalie, R., Wigneron, J.-P., 2019. Uncertainty in soil moisture retrievals: an ensemble approach using SMOS L-band microwave data. Remote Sens. Environ. 229, 133–147.
Rautiainen, K., Lemmetyinen, J., Pulliainen, J., Vehvilainen, J., Drusch, M., Kontu, A., Kainulainen, J., Seppanen, J., 2012. L-band radiometer observations of soil processes in boreal and subarctic environments. IEEE Trans. Geosci. Remote Sens. 50, 1483–1497.
Rodriguez-Fernández, N.J., Mialon, A., Mermoz, S., Bouvet, A., Richaume, P., Al Bitar, A., Al-Yaari, A., Brandt, M., Kaminski, T., Le Toan, T., Kerr, Y.H., Wigneron, J.-P., 2018. An evaluation of SMOS L-band vegetation optical depth (L-VOD) data sets: high sensitivity of L-VOD to above-ground biomass in Africa. Biogeosciences. 15, 4627–4645.
Saatchi, S.S., Harris, N.L., Brown, S., Lefsky, M., Mitchard, E.T.A., Salas, W., Zutta, B.R., Buermann, W., Lewis, S.L., Hagen, S., Petrova, S., White, L., Silman, M., Morel, A., 2011. Benchmark map of forest carbon stocks in tropical regions across three continents. Proc. Natl. Acad. Sci. 108 (24), 9899–9904.
Sadeghi, M., Gao, L., Ebtehaj, A., Wigneron, J.-P., Crow, W.T., Reager, J.T., Warrick, A. W., 2020. Retrieving global surface soil moisture from GRACE satellite gravity data. J. Hydrol. 584, 124717.
Saleh, K., Wigneron, J.-P., De Rosnay, P., Calvet, J.-C., Escorihuela, M.J., Kerr, Y., Waldteufel, P., 2006. Impact of rain interception by vegetation and mulch on the L-band emission of natural grass. Remote Sens. Environ. 101 (1), 127–139.
Sanchez, N., Martínez-Fernández, J., Scaini, A., Perez-Gutierrez, C., 2012. Validation of the SMOS L2 soil moisture data in the REMEDHUS network (Spain). IEEE Trans. Geosci. Remote Sens. 50, 1602–1611.
Santoro, M., Cartus, O., Mermoz, S., Bouvet, A., Le Toan, T., Carvalhais, N., Rozendaal, D., Herold, M., Avitabile, V., Quegan, S., Carreiras, J., Rauste, Y., Balzter, H., Schmullius, C., Seifert, F.M., 2018. A detailed portrait of the forest aboveground biomass pool for the year 2010 obtained from multiple remote sensing observations. Geophys. Res. Abstr. 20. EGU2018–18932.
Schaefer, G.L., Cosh, M.H., Jackson, T.J., 2007. The USDA natural resources conservation service soil climate analysis network (SCAN). J. Atmos. Ocean. Technol. 24, 2073–2077.
Scholze, M., Kaminski, T., Knorr, W., Vossbeck, M., Wu, M., Ferrazzoli, P., Kerr, Y., Mialon, A., Richaume, P., Rodriguez-Fernandez, N., Vittucci, C., Wigneron, J.-P., Mecklenburg, S., Drusch, M., 2019. Mean European carbon sink over 2010–2015 estimated by simultaneous assimilation of atmospheric CO2, soil moisture, and vegetation optical depth. Geophys. Res. Lett. 46.
Serreze, M.C., Clark, M.P., Frei, A., 2001. Characteristics of large snowfall events in the montane western United States as examined using snowpack telemetry (SNOTEL) data. Water Resour. Res. 37, 675–688.
Shi, J., Dong, X., Zhao, T., Du, Y., Liu, H., Wang, Z., Zhu, D., Ji, D., Xiong, C., Jiang, L., WCOM, 2016. The water cycle observation mission (WCOM): Overview. IEEE Intern. Geosci. Remote Sens. Symp. (IGARSS), Beijing 3430–3433.
Slatyer, R.O., 1967. Plant-Water Relationships. New York.
Soldo, Y., Khazaal, A., Cabot, F., Kerr, Y.H., 2016. An RFI index to quantify the contamination of SMOS data by radio-frequency interference. IEEE J. Sel. Top. Appl. Earth Observ. Remote Sens. 9 (4), 1577–1589.
Smith, A., Walker, J.P., Western, A.W., Young, R., Ellett, K., Pipunic, R., Grayson, R., Siriwardena, L., Chiew, F., Richter, H., 2012. The Murrumbidgee soil moisture monitoring network data set. Water Resour. Res. 48.
Tagesson, T., Fensholt, R., Guiro, I., Rasmussen, M.O., Huber, S., Mbow, C., Garcia, M., Horion, S., Sandholt, I., Holm-Rasmussen, B., et al., 2015. Ecosystem properties of semiarid savanna grassland in West Africa and its relationship with environmental variability. Glob. Chang. Biol. 21, 250–264.
Tagesson, T., Schurgers, G., Horion, S., Ciais, P., Tian, F., Brandt, M., Ahlström, A., Wigneron, J.-P., Ardö, J., Olin, S., Fan, L., Wu, Z., Fensholt, R., 2020. Recent Divergence in the Contributions of Tropical and Boreal Forests to the Terrestrial Carbon Sink, 4, pp. 202–209.
Tian, F., Wigneron, J.-P., Ciais, P., Chave, J., Ogée, J., Peñuelas, J., Ræbild, A., Domec, J.-C., Tong, X., Brandt, M., Mialon, A., Rodriguez-Fernandez, N., Tagesson, T., Al-Yaari, A., Kerr, Y., Chen, C., Myneni, R.B., Zhang, W., Ardö, J., Fensholt, R., 2018. Coupling of ecosystem-scale plant water storage and leaf phenology observed by satellite. Nat. Ecol. Evol. 2, 1428–1435.
Tong, X., Brandt, M., Yue, Y., Ciais, P., Rudbeck Jepsen, M., Penuelas, J., Wigneron, J.-P., Xiao, X., Song, X.-P., Horion, S., Rasmussen, K., Saatchi, S., Fan, L., Wang, K., Zhang, B., Chen, Z., Wang, Y., Li, X., Fensholt, R., 2020. Forest management in southern China generates short term extensive carbon sequestration. Nat. Commun. 13798-8.
Wigneron, J.P., Chanzy, A., Calvet, J.C., Bruguier, N., 1995. A simple algorithm to retrieve soil moisture and vegetation biomass using passive microwave measurements over crop fields. Remote Sens. Environ. 51, 331–341.

Wigneron, J.-P., Waldteufel, P., Chanzy, A., Calvet, J.-C., Kerr, Y., 2000. Two-D microwave interferometer retrieval capabilities of over land surfaces (SMOS Mission). Remote Sens. Environ. 73, 270–282.
Wigneron, J.-P., Calvet, J.-C., Pellarin, T., Van de Griend, A., Berger, M., Ferrazzoli, P., 2003. Retrieving near surface soil moisture from microwave radiometric observations: current status and future plans. Remote Sens. Environ. 85, 489–506.
Wigneron, J.-P., Pardé, M., Waldteufel, P., Chanzy, A., Kerr, Y., Schmidl, S., Skou, N., 2004. Characterizing the dependence of vegetation model parameters on crop structure, incidence angle, and polarization at L-band. IEEE Trans. Geosci. Remote Sens. 42 (2), 416–425.
Wigneron, J.-P., Kerr, Y., Waldteufel, P., Saleh, K., Escorihuela, M.J., Richaume, P., Ferrazzoli, P., de Rosnay, P., Gurney, R., Calvet, J.C., Grant, J.P., Guglielmetti, M., Hornbuckle, B., Mätzler, C., Pellarin, T., Schwank, M., 2007. L-band microwave emission of the biosphere (L-MEB) model: description and calibration against experimental data sets over crop fields. Remote Sens. Environ. 107, 639–655.
Wigneron, J.-P., Schwank, M., Lopez Baeza, E., Kerr, Y.H., Novello, N., Millan, C., Moisy, C., Richaume, P., Mialon, A., Al Bitar, A., Cabot, F., Lawrence, H., Guyon, D., Calvet, J.-C., Grant, J.P., Casal, T., de Rosnay, P., Saleh, K., Mahmoodi, A., Delwart, S., Mecklenburg, S., 2012. First evaluation of the SMOS observations over the VAS site in the Mediterranean region. Remote Sens. Environ. 124, 26–37.
Wigneron, J.-P., Jackson, T.J., O'Neill, P., De Lannoy, G., de Rosnay, P., Walker, J.P., Ferrazzoli, P., Mironov, V., Bircher, S., Grant, J.P., Kurum, M., Schwank, M., Munoz-Sabater, J., Das, N., Royer, A., Al-Yaari, A., Al Bitar, A., Fernandez-Moran, R., Lawrence, H., Mialon, A., Parrens, M., Richaume, P., Delwart, S., Kerr, Y., 2017. Modelling the passive microwave signature from land surfaces: a review of recent results and application to the L-band SMOS & SMAP soil moisture retrieval algorithms. Remote Sens. Environ. 192, 238–262.
Wigneron, J.-P., Mialon, A., De Lannoy, G., Fernandez-Moran, R., Al-Yaari, A., Ebrahimi, M., Rodriguez-Fernandez, N., Kerr, Y., Quets, J., Pellarin, T., Fan, L., Tian, F., Fensholt, R., Brandt, M., 2018. SMOS-IC: Current status and overview of soil moisture and VOD applications. In: IGARSS 2018, 2018 IEEE International Geoscience and Remote Sensing Symposium, pp. 1451–1453.
Wigneron, J.-P., Fan, L., Ciais, P., Bastos, A., Brandt, M., Chave, J., Saatchi, S., Baccini, A., Fensholt, R., 2020. Tropical forests did not recover from the strong 2015–2016 El Niño event. Sci. Adv. 6 (6), eaay4603.
Yang, H., Ciais, P., Santoro, M., Huang, Y., Li, W., Wang, Y., Bastos, A., Goll, D., Arneth, A., Anthoni, P., Arora, V.K., Friedlingstein, P., et al., 2020. Comparison of forest above-ground biomass from dynamic global vegetation models with spatially explicit remotely sensed observation-based estimates. Glob. Chang. Biol. 26 (7), 3997–4012.
Zeng, J., Li, Z., Chen, Q., Bi, H., Qiu, J., Zou, P., 2015. Evaluation of remotely sensed and reanalysis soil moisture products over the Tibetan plateau using in-situ observations. Remote Sens. Environ. 163, 91–110.
Zhang, R., Kim, S., Sharma, A., Lakshmia, V., 2020. Identifying relative strengths of SMAP, SMOS-IC, and ASCAT to capture temporal variability. Remote Sens. Environ. 252, 112126.
Zhang, Y., Zhou, S., Gentine, P., Xiao, X., 2019. Can vegetation optical depth reflect changes in leaf water potential during soil moisture dry-down events? Remote Sens. Environ. 234, 111451.